# Serendipitous infrared observations of Europa by Juno/JIRAM

Gianrico Filacchione[a,*], Alberto Adriani[a], Alessandro Mura[a], Federico Tosi[a], Jonathan I. Lunine[b], Andrea Raponi[a], Mauro Ciarniello[a], Davide Grassi[a], Giuseppe Piccioni[a], Maria Luisa Moriconi[a], Francesca Altieri[a], Christina Plainaki[c], Giuseppe Sindoni[c], Raffaella Noschese[a], Andrea Cicchetti[a], Scott J. Bolton[d], Shawn Brooks[e]

[a] *INAF-IAPS, Istituto di Astrofisica e Planetologia Spaziali, Area di Ricerca di Tor Vergata, via del Fosso del Cavaliere, 100, 00133, Rome, Italy*
[b] *Cornell University, Ithaca, NY, USA.*
[c] *ASI, Agenzia Spaziale Italiana, via del Politecnico, snc, 00133, Rome, IT.*
[d] *Space Science and Engineering Division, Southwest Research Institute, San Antonio, TX, USA.*
[e] *NASA-JPL, Pasadena, CA, USA.*

## Abstract

We performed spectral analyses on four serendipitous observations of Europa acquired by the JIRAM instrument (*Adriani et al.*, 2017) onboard the Juno mission. Due to the fixed orientation of the spacecraft spin axis and orbital plane placed along terminator, Europa is observed at approximately 90° phase angle from distances greater than 3.35E5 km resulting in a best spatial resolution of 80 km/px. The one thousand spectra dataset returned to the ground offers a limited coverage in longitude but an almost complete excursion in latitude from poles to equator. With a 2 to 5 $\mu$m spectral range and a sampling of about 10 nm/band, JIRAM reflectance spectra allow extraction of different spectral indicators suitable to characterize surface composition, grain size distribution and temperature: the 2 $\mu$m water ice band center appears on average centered at 2.038 $\mu$m as a result of the presence of both amorphous and crystalline ice phases and non-ice materials. The reflectance level on the 2.4 $\mu$m inflection shoulder is comparable to the maximum absorption on the 2 $\mu$m band pointing to the presence of non-ice materials, like magnesium chlorinated or hydrated magnesium salts, mixed with water ice. Assuming water ice as the principal endmember, we estimate the surface regolith grain size by comparing the 2

*Corresponding author, email gianrico.filacchione@inaf.it

$\mu$m band depth and the ratio between I/F at 3.63 and 2.27 $\mu$m (*Filacchione et al.*, 2012). On average, we measure values of 0.6 for the first and 0.1 for the latter: such values are compatible with grain sizes in the range of tens to hundreds of microns. Despite the low signal-to-noise beyond 2.7 $\mu$m, due to the intrinsic low-reflectance of Europa's surface and very high phase angle values occurring during the observations, JIRAM is able to measure the wavelength of the reflectance peak around 3.6 $\mu$m, which is a proxy of water ice temperature (*Filacchione et al.*, 2016a). In the dataset JIRAM has obtained the peak's maximum wavelength occurs at 3.64 $\mu$m corresponding to a maximum diurnal temperature of 132 K.

*Keywords:* Europa, Satellites, surfaces, Spectroscopy, Ices

## 1. Introduction

Despite the Galilean moons not being among the nominal scientific objectives of NASA's Juno mission to Jupiter (*Bolton and Connerney*, 2017), JIRAM the Jovian InfraRed Auroral Mapper (*Adriani et al.*, 2017) was able to observe the surface of Europa during four opportunities. In the context of an overall program of "ocean worlds" exploration, the data returned by JIRAM are valuable for better constraining the characteristics of the moon's surface in the 2-5 $\mu$m spectral range. In the past, Europa's surface has been spectrally mapped at these wavelengths only by three interplanetary missions. So far, Galileo/NIMS (*Carlson et al.*, 1992) has returned the more comprehensive dataset despite being limited to partial coverage of the surface. These data have allowed mapping of the distribution of non-ice materials, mainly identified as hydrated sulfuric acid, which appear more abundant on the trailing hemisphere (*Carlson et al.*, 2005) and hydrated salts (magnesium sulfates, sodium carbonates) associated with the low-albedo areas (*McCord et al.*, 1998, 1999). Also Cassini/VIMS (*Brown et al.*, 2004) during its flyby of Jupiter in 2000 was able to perform limited observations of Europa's surface at low spatial resolution in the 0.35-5.0 $\mu$m range (*Brown et al.*, 2003; *McCord et al.*, 2004). Similarly, LEISA spectrometer (*Reuter et al.*, 2008) on New Horizon has returned re-

solved spectra of Europa's surface (*Grundy et al.*, 2007) in the 1.2-2.5 $\mu$m range. For the future, Europa will be the target of NASA's Europa Clipper and ESA's Juice missions, both planned to start their scientific investigations in the 2030 timeframe. These missions will have aboard dedicated infrared mapping spectrometers covering the same spectral range of JIRAM: Europa Clipper/MISE (Mapping Imaging Spectrometer for Europa, described in *Blaney et al.* (2017)) and JUICE/MAJIS (Moon And Jupiter Imaging Spectrometer, detailed in *Langevin et al.* (2014)). Since the 2-5 $\mu$m spectral range is scarcely accessible from Earth-telescopes, JIRAM data are of special value in providing an advanced look at the kind of spectra these other mission will obtain.

A discussion of the current knowledge of Europa's surface spectral properties is given in section 2. Section 3 contains a description of the JIRAM instrument's architecture and operative mode necessary for a comprehension of Europa's observations which are detailed in section 4. After a description of the spectral indicators used to analyze JIRAM data (section 5), the main results relative to compositional properties (section 6), regolith grain size (section 7), water ice amorphization (section 8) and temperature retrieval (section 9) are exposed. A discussion about JIRAM results in the context of previous observations is given in section 10.

## 2. Background

Europa is one of the four Galilean moons, the regular satellites of Jupiter named after Galileo Galilei who observed them for the first time on the night of January 7th 1610. With an average radius of 1560 km and a geometric albedo of 0.67 (*Buratti et al.*, 1983), Europa is the smallest and the brightest object among the four regular moons. The surface of Europa appears geologically young, with a crust made of water ice and nonice compounds floating above a subsurface liquid ocean (*Greenberg*, 2005).

Crossing through the surface are visible dark markings, called linea, and chaos terrains generated by tidal movements below the ice shell with consequent resurfacing and exposure

of nonice materials. Infrared spectroscopic measurements have shown that europan nonice material has similarities with magnesium salts (*McCord et al.*, 1998, 1999) and sulfuric acid-rich compounds (*Carlson et al.*, 2005). The presence of salts is a clue to the presence of environmental conditions favorable to life in the subsurface ocean (*Fanale et al.*, 2001; *Hand et al.*, 2007) while sulfur-bearing compounds could result from radiolytic processes altering endogenous materials (*Carlson et al.*, 1999b, 2002) or magnetospheric particles (*Dalton et al.*, 2005, 2012).

Galileo/NIMS spectra evidence that water ice is distributed across Europa's surface in both the crystalline and amorphous state (*Carlson et al.*, 2009). Crystalline ice forms in metastable cubic lattice at temperature $140 \leq T \leq 150$ K while disordered amorphous ice forms condense at T$\leq$ 30K (high-density ice phase), T$\leq$ 100K (low-density ice phase) or at $100 \leq T \leq 140$ K (restrained phase). The latter can coexist with the crystalline cubic type when the temperature is $T \leq 140$ K (*Jenniskens et al.*, 1998). With aging, these water ice types eventually mutate into crystalline hexagonal ice with transformation rates that depend on temperature. Within the range of temperatures observed on Europa's surface (minimum nocturnal T$\leq$76 K; maximum diurnal T=132 K, *Spencer et al.* (1999)), one would expect that all amorphous ice would be transformed into hexagonal ice in less than 20 years (*Jenniskens et al.*, 1998).

The crystalline and amorphous water ices can be recognized thanks to their different spectral properties at infrared wavelengths. In particular, the crystalline form is characterized by the presence of a secondary absorption at 1.65 $\mu$m (missing in the amorphous ice) within the intense 1.5 $\mu$m band, by the position of the 2.05 $\mu$m band (shifted at 2.0 $\mu$m in the amorphous ice) and by the 3.1 $\mu$m Fresnel's reflectance peak properties. The Fresnel's peak is a restrahlen feature which occurs at wavelengths where the absorption is so strong that the medium reflects the light like a metal. For water ice this feature appears broad and weak for the amorphous phase while is narrower and structured like a triplet for cold crystalline ice (*Hagen et al.*, 1981).

As said before, since the Europa's environmental temperature conditions do not allow the

survival of amorphous ice, additional mechanisms able to continuously refurbish it must be acting. Amorphous ice can be formed by condensation of sublimated and sputtered molecules and by irradiation from UV, electrons and ions. Many laboratory experiments have investigated how the effects of different kind of radiations at different temperature ranges alter water ice molecular structure (*Moore and Hudson*, 1992; *Leto and Baratta*, 2003; *Baragiola*, 2003; *Leto et al.*, 2005; *Mastrapa and Brown.*, 2006). However, since the radiation is attenuated within the medium, the resulting amorphization of the ice should occur only on a relatively shallow surface layer. For electrons, for example, theoretical models show that radiation processing occurs up to depths of 1 cm in mid and high latitude regions of Europa and up to 10-20 cm in the radiation lenses centered on the apex of the leading and training hemispheres (*Nordheim et al.*, 2018). This effect must be kept in mind when spectral results are analyzed. The retrieval of the water ice state from infrared spectral properties ($k$ being the complex index of refraction) is complicated because the absorption coefficient $\alpha(\lambda) = 4\pi k(\lambda)/\lambda$ is wavelength-dependent (*Lynch*, 2005). The optical skin depth, $1/\alpha(\lambda)$, which corresponds to unitary optical depth, $\tau$, is less than 1 $\mu$m at the wavelength of the Fresnel's peak while at 2 $\mu$m is less than 10 cm. This means that using these two wavelengths one is probing different depths within the surface layer. A similar behavior is recognizable in *Hansen and McCord* (2004) work who have exploited a simplified spectral modeling to map water ice forms across Europa's surface using Galileo/NIMS data. Their findings show that crystalline water ice is able to fit the 1.5 and 2.0 $\mu$m bands while amorphous ice is necessary to reproduce the spectral behavior observed on the Fresnel's peak: the fact that amorphous ice is observed almost everywhere across Europa's surface is a strong indication that the Fresnel's peak properties are easily altered by radiations and thermal effects occurring in a very shallow water ice layer. Noteworthy, the Fresnel peak is also influenced when water ice is contaminated by nonice materials, e.g. it is removed in hydrated materials spectra (*Carlson et al.*, 2009).

New Horizon/LEISA has retrieved the 2 $\mu m$ water ice band depth and nonice material

abundance maps which appear anti-correlated among them: the first is relatively constant, between 35% to 60% in the regions less contaminated by nonice material, while the latter reaches maximum abundance on the apex of the trailing hemisphere (*Grundy et al.*, 2007). While LEISA data are limited in coverage to regions at latitudes $\leq+60°$, a better view of the north polar regions has been achieved by Galileo/NIMS whose data show a water ice enrichment across the north pole bright plains (*Fanale et al.*, 1999). Galileo NIMS has also identified other species like hydrogen peroxide ($H_2O_2$) by observing a faint absorption band at 3.5 $\mu$m (*Carlson et al.*, 1999a), sulfur dioxide's 4.03 $\mu$m feature (*McCord et al.*, 1998; *Carlson et al.*, 2009) and $CO_2$ ice's 4.26 $\mu$m band (*Hansen and McCord*, 2008). A further absorption at 3.78 $\mu$m, possibly associated to sulfur dioxide, has been observed by NIRSPEC on the Keck II telescope (*Trumbo et al.*, 2018).

Independent analyses of Europa's infrared spectra (*Hansen and McCord*, 2004; *Dalton et al.*, 2012; *Ligier et al.*, 2016) and polarimetric data (*Poch et al.*, 2018) aiming to the retrieval of the regolith grain size have shown a distribution within tens and hundreds of microns. The presence of $>100$ $\mu$m grains make the europan surface distinctively different with respect to other icy satellites, like those of Saturn, in which very small grains dominate: according to *Stephan et al.* (2010, 2012, 2016); *Scipioni et al.* (2017) the surfaces of the icy satellites of Saturn are populated by submicron and micron ($< 5$ $\mu$m) grains. Other authors (*Verbiscer et al.*, 2006; *Filacchione et al.*, 2012; *Ciarniello et al.*, 2011) have found larger grain size distributions ($<$ 80 $\mu$m) but still smaller than those on Europa. Similar discrepancies between grain sizes may be due to the different spectral models employed in the retrieval as has been demonstrated by published comparisons (*Hansen*, 2009; *Shkuratov et al.*, 2012; *Ciarniello et al.*, 2014).

While ongoing or recent evolution is seen on all Galilean satellites surfaces, including the resurfaced and chaos terrains on Europa, thermal sintering and bombardment of energetic particles induced by the high Jovian temperatures and radiation environment might be the cause of grain coalescence up to hundred of micron sizes. These effects are more important in

the Jupiter's environment than at Saturn where temperature and radiation effects are much lower. Apart from this, Saturn's satellites orbiting within the E-ring boundaries are also affected by the deposition of fine grains from Enceladus' plume (*Porco et al.*, 2006) which contribute to replenish micron and submicron grains on their surfaces.

When temperatures exceeds 100 K, such as on Europa's dayside, water ice grains have higher mobility which would cause sintering, coalescence and growth (*Gundlach et al.*, 2018; *Häßner et al.*, 2018). A similar mechanism is probable at the base of the formation of the larger grains observed on Europa's surface but also in other water ice-rich environments, such as the surface of comets (*Filacchione et al.*, 2016b).

## 3. JIRAM instrument

JIRAM is an advanced infrared imaging spectrometer and camera operating on board the Juno mission specifically designed to observe Jupiter's atmosphere (*Adriani et al.*, 2018) and auroral emissions (*Mura et al.*, 2018). The instrument shares a single telescope to feed a 2-5 $\mu$m imaging spectrometer and a dual-band infrared camera through a beam splitter. The spectrometer (SPE) spectral sampling is about 10 nm/band across a field of view (FOV) of 3.67°. A 2D HgCdTe detector is used to acquire a 256 samples by 336 bands frame. The imager (IMG) relies on a push-frame design in which a single array detector observes the scene through two filters in band L ($\lambda$=3.455 $\mu$m, $\Delta\lambda$=0.29 $\mu$m) and M ($\lambda$=4.780 $\mu$m, $\Delta\lambda$=0.48 $\mu$m). The L band is optimized for the observation of Jupiter's auroral emissions caused by $H_3^+$ emissions, while the M band is devoted to observe the Jovian atmospheric thermal emission. Both L and M channels have a field of view of 6.2° × 1.8° imaged by means of two adjacent 432 × 128 pixels areas arranged side by side on a 270 by 438 pixels detector. The instantaneous field of view (IFOV) of both IMG and SPE channels is 250 $\mu$rad/pixel resulting in a spatial resolution of 250 km/pixel from one million km distance. The FOV of the SPE channel is co-located within the IMG-M channel and oriented parallel to the spacecraft spin axis to optimize the

coverage. Finally, the instrument uses a passive thermal design to reach cryogenic operating temperatures: two external radiators are used to dissipate thermal loads necessary to maintain the optical bench at T=130 K and the two detectors at T$\leq$85K. A comprehensive description of the JIRAM instrument is given in *Adriani et al.* (2017).

A major challenge for any imaging instrument onboard a spinning spacecraft is the compensation of the rotation during the period of time necessary to acquire an image. In the case of Juno, the spacecraft is a spin axis-stabilized platform with an angular rotation of about 2 r.p.m. (12°/s) placed on highly elliptical, 53.5 day-long, polar orbits around Jupiter (*Bolton and Connerney*, 2017). Due to operational constraints, JIRAM can operate only in a limited period of time, spanning between -13 to + 2 hours around perijovian passage (occurring at 4.200 km above the top of Jupiter's clouds), when the relative velocity of the spacecraft with respect to Jupiter reaches values as high as 60 km/s. JIRAM is able to counter-compensate the spacecraft's rotation by means of a controlled de-spinning mirror placed at the entrance of the telescope. The mirror rotation axis is oriented parallel to the spacecraft rotation axis. During acquisition, the de-spinning mirror is commanded to rotate with an angular velocity equal and opposite to the spacecraft one. The spacecraft angular velocity and clock (relative to the condition of nadir pointing on Jupiter) is determined by the onboard attitude control and transmitted to the JIRAM instrument at every spacecraft rotation. The mirror parameters (angular offset, timing and angular velocity) as well as the acquisition parameters of the SPE and IMG channels (timing, integration times, operative modes) are commanded to capture scientific targets when transiting through the instrumental FOV. Thanks to this architecture it is possible to freeze the scene within the FOV for a maximum time of 1.2 s. for each 30 s. long spacecraft rotation. During each rotation JIRAM can acquire one hyperspectral slit in the 2-5 $\mu$m spectral range with the SPE channel and one image in L and/or M band with the IMG channel. However, while JIRAM-SPE is in principle able to build in time hyperspectral images, in practice it cannot operate in imaging mode, because the time resolution necessary

to acquire consecutive adjacent slits is far beyond the possibilities of the onboard attitude and timing system due to the fast dynamics of the Juno's spacecraft. A description of JIRAM science planning and commanding activities is given in *Noschese et al.* (under review).

Since the spacecraft's on board attitude system has been designed and optimized to allow scientific observations of Jupiter but not of the Galilean satellites, which are not among the objectives of the Juno mission, the acquisition of Europa's spectra are particularly challenging. One of the major difficulties encountered is the timing of the observations because the onboard attitude system has been designed to provide the clock of the nadir-pointing condition during each spacecraft rotation only for Jupiter and not for the satellites. This means that to observe them is necessary to compute a priori the time and angle offsets (including margins) to command JIRAM acquisitions. Despite these limitations, JIRAM team has exploited the instrument capabilities far beyond the nominal science cases in order to observe the Galilean moons, resulting in the acquisition of the serendipitous dataset of Europa presented in the next section 4.

## 4. Dataset and calibration

JIRAM has successfully observed Europa's surface during Juno's orbits #2 (August 2nd-3th 2016), #8 (September 1st 2017), #9 (October 25th 2017) and #11 (February 8th 2018) when Europa's orbital position was crossing Juno's orbital plane. The resulting dataset is listed in Table 1. The duration of the acquisitions, grouped into sessions, is driven by the time necessary to observe a transit of Europa within the JIRAM-SPE field of view. The spectrometer's data show Europa's disk crossing the length of the slit from one side to the other. In each session JIRAM has acquired consecutive images and spectra taken once every 30 s, i.e. every spacecraft rotation. Due to the limitations explained in section 3, it was impossible to acquire connected slits to build hyperspectral images; instead they are randomly dispersed across the surface. The geometric parameters for each observation reported in Table 1 are derived from trajectory-

| Session | Latitude (deg) | | Longitude (deg) | | Incidence (deg) | | Emission (deg) | | Phase (deg) | | Resolution | # spectra |
|---|---|---|---|---|---|---|---|---|---|---|---|---|
| Orbit-Date-Time | min | max | min | max | min | max | min | max | min | max | (km/pix) | |
| JM0002_160802_213108 | 22.3 | 27.0 | 133.0 | 144.7 | 88.1 | 98.6 | 27.3 | 29.3 | 86.2 | 86.2 | 1809 | 19 |
| JM0002_160803_010100 | 0.5 | 66.4 | 75.7 | 217.3 | 14.5 | 151.9 | 10.8 | 83.4 | 87.3 | 87.3 | 1781 | 19 |
| JM0081_170901_105708 | 20.6 | 24.0 | 37.4 | 40.8 | 28.5 | 28.5 | 73.4 | 73.4 | 91.5 | 91.5 | 88 | 4 |
| JM0081_170901_110210 | 2.2 | 87.5 | 7.1 | 288.7 | 19.8 | 94.8 | 21.9 | 85.8 | 91.4 | 91.6 | 87 | 3 |
| JM0081_170901_110711 | 2.0 | 82.2 | 12.7 | 357.6 | 28.1 | 160.8 | 16.7 | 78.2 | 91.3 | 91.7 | 87 | 8 |
| JM0081_170901_111213 | -3.6 | 79.3 | 9.9 | 358.7 | 23.6 | 162.6 | 15.5 | 83.7 | 91.4 | 91.9 | 86 | 9 |
| JM0081_170901_111715 | 1.8 | 74.4 | 0.8 | 351.7 | 22.6 | 169.0 | 12.1 | 88.4 | 91.5 | 92.0 | 85 | 10 |
| JM0081_170901_112216 | 7.0 | 72.7 | 3.9 | 356.4 | 25.3 | 169.5 | 11.4 | 82.4 | 91.7 | 92.1 | 84 | 8 |
| JM0081_170901_112718 | 3.9 | 67.9 | 0.2 | 354.0 | 22.5 | 162.7 | 11.0 | 84.7 | 91.8 | 92.3 | 84 | 9 |
| JM0081_170901_113219 | -11.8 | 67.1 | 1.5 | 357.4 | 22.0 | 169.7 | 5.1 | 85.1 | 91.9 | 92.4 | 83 | 7 |
| JM0081_170901_113651 | 4.8 | 77.8 | 3.9 | 352.5 | 30.3 | 158.7 | 23.9 | 76.1 | 92.1 | 92.6 | 83 | 12 |
| JM0081_170901_114152 | 5.3 | 75.1 | 1.0 | 351.4 | 28.5 | 162.9 | 22.3 | 85.8 | 92.2 | 92.7 | 82 | 10 |
| JM0081_170901_114654 | 2.8 | 67.8 | 4.8 | 359.1 | 27.6 | 169.8 | 16.7 | 86.4 | 92.4 | 92.8 | 81 | 9 |
| JM0081_170901_115156 | 7.9 | 67.8 | 3.1 | 357.1 | 30.4 | 161.8 | 17.5 | 85.4 | 92.5 | 93.0 | 81 | 14 |
| JM0081_170901_115657 | 10.5 | 63.8 | 4.0 | 359.5 | 28.0 | 165.3 | 13.4 | 78.5 | 92.7 | 93.1 | 81 | 10 |
| JM0081_170901_120159 | 6.9 | 67.5 | 1.3 | 357.0 | 27.5 | 174.0 | 10.7 | 82.6 | 92.8 | 93.3 | 80 | 7 |
| JM0081_170901_120700 | 9.2 | 68.7 | 0.4 | 356.2 | 72.5 | 172.3 | 10.6 | 80.2 | 93.0 | 93.3 | 80 | 4 |
| JM0091_171025_000341 | -8.4 | -0.4 | 36.4 | 44.2 | 32.1 | 39.9 | 61.4 | 72.3 | 87.8 | 87.9 | 135 | 6 |
| JM0091_171025_001317 | -89.2 | 17.7 | 0.4 | 358.4 | 15.6 | 159.9 | 12.5 | 86.9 | 88.2 | 88.8 | 135 | 24 |
| JM0091_171025_002324 | -87.0 | 25.9 | 4.2 | 358.8 | 7.18 | 156.4 | 2.5 | 87.6 | 89.6 | 90.0 | 135 | 15 |
| JM0091_171025_003331 | -81.2 | 17.2 | 1.5 | 356.4 | 28.8 | 161.3 | 5.6 | 80.8 | 91.0 | 91.3 | 136 | 11 |
| JM0111_180208_054729 | -80.0 | -14.3 | 1.2 | 356.9 | 46.0 | 152.1 | 31.1 | 86.7 | 84.5 | 85.3 | 186 | 42 |
| JM0111_180208_055735 | -84.3 | -19.4 | 0.4 | 358.8 | 37.2 | 151.6 | 26.8 | 85.1 | 85.2 | 86.0 | 186 | 46 |
| JM0111_180208_060741 | -85.8 | -13.8 | 1.8 | 359.3 | 37.4 | 155.1 | 24.2 | 88.4 | 86.0 | 86.7 | 187 | 27 |
| JM0111_180208_061717 | -89.3 | -9.6 | 1.8 | 359.7 | 31.1 | 156.8 | 21.1 | 88.2 | 86.6 | 87.4 | 188 | 51 |
| JM0111_180208_062723 | -88.9 | -17.8 | 0.4 | 359.8 | 38.7 | 158.2 | 19.9 | 81.6 | 87.4 | 88.1 | 188 | 36 |

Table 1: List of Europa's JIRAM-SPE observations and geometry parameters.

reconstructed SPICE kernels (*Acton*, 1996). All Europa observations are acquired with the maximum integration time of 1.2 s. Noteworthy, attitude-reconstructed SPICE kernels for the Juno mission do not include spacecraft's nutation and precession effects, resulting in further uncertainty in the retrieval of the instrumental FOV position on Europa's surface. In addition, JIRAM-IMG has collected multiple images covering the entire disk of Europa (see Fig. 2 for an example) at the same time of the SPE acquisitions. Within the JIRAM dataset the minimum and maximum altitude of Juno from Europa ranges between 3.3E5 km and 7.6E6 km corresponding to spatial resolution between 80 and 1809 km/pixel, respectively. Due to the characteristics of Juno's trajectory, Europa is always observed by JIRAM with a solar phase angle of approximately 90°.

The aforementioned limitations in retrieving georeferenced data prevent us from producing

maps with accurate locations of JIRAM-SPE pixels. Thus, our results are discussed in terms of localization across wide sectors of Europa's surface, being only capable of identifying the position of the illuminated pixels at hemispheric scale. The regions of the surface visible from Juno at the time of JIRAM acquisitions are reported in Fig. 1. The observations taken during orbits JM0002-JM0081 contain data collected above the northern hemisphere while the second two (JM0091-JM0111) are mainly taken above the southern regions. During orbit JM0002 JIRAM has achieved a good coverage above the northern/antijovian hemisphere despite those data being limited by the worst spatial resolution of the dataset (1781-1809 km/pixel). The northern/jovian hemisphere together with a portion of the trailing hemisphere are both covered during orbit JM0081 with the best spatial resolution of the dataset (80-88 km/pixel). The coverage achieved during orbits JM0091-JM0111 is limited around lon=0° from the equatorial regions to the south pole with spatial resolution of 135-188 km/pixel.

The raw signal of each JIRAM acquisition is corrected pixel by pixel for the instrument background and detector's dark current noises measured on a deep sky field with the same integration time of the science data. The onboard software operates automatically the subtraction of the noises before the data are transmitted on-ground (*Adriani et al.*, 2017). With respect to the standard JIRAM calibration pipeline that produces data calibrated in units of spectral radiance, the SPE data are further processed to: 1) remove the non-linear readout noise (high frequency noise between odd and even spectral bands) introduced by the detector's multiplexer (*Filacchione et al.*, 2007); 2) to convert radiance into I/F units. The odd-even effect is removed by applying the following correction on the spectral radiance R measured at band b:

$$R_c(b) = \frac{R(b) + \frac{R(b-1)+R(b+1)}{2}}{2} \tag{1}$$

The resulting corrected radiance, $R_c$, is used to derive the I/F at wavelength $\lambda$:

$$\frac{I}{F}(\lambda) = \frac{4\pi D^2 R_c(\lambda)}{SI(\lambda)} \tag{2}$$

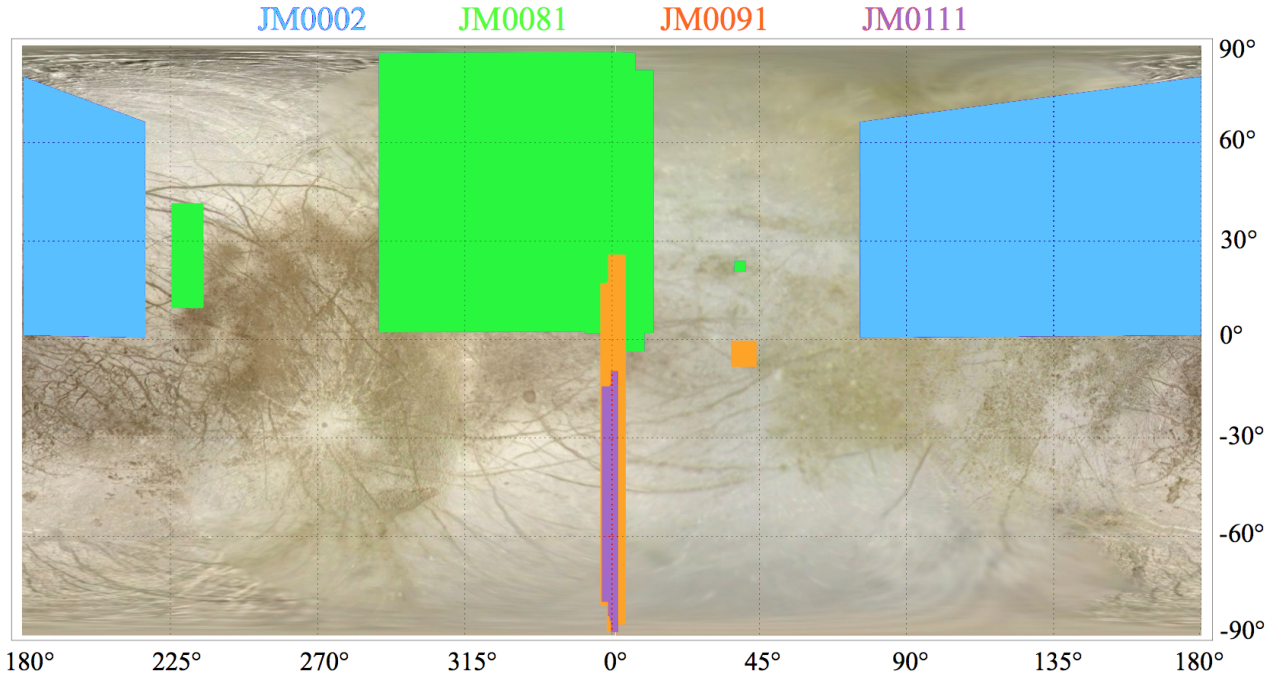


Figure 1: Europa's surface coverage on the JIRAM-SPE dataset shown on a cylindrical map of the satellite. The fraction of the surface containing the positions of JIRAM's slit projections during orbits JM0002 (rendered in blue color), JM0081 (green), JM0091 (orange) and JM0111 (purple) is shown. The base map is derived from Voyager and Galileo images (by Björn Jonsson, available from `http://www.mmedia.is/bjj/`).

where $SI(\lambda)$ is the solar irradiance measured at 1 AU (*Kurucz*, 1994) and D is Europa's heliocentric distance (in AU) at the time of the observation.

With the scope to optimize the spectral analysis, we have filtered Europa's spectra by selecting only the ones having I/F(2.227 $\mu$m) $\geq$ 0.01. This selection allows to remove low-signal spectra like the ones across limb or terminator where JIRAM pixels are only partially filled. As a result of this filtering, the initial dataset of about one thousand I/F spectra is reduced to 419 spectra shown as a spectrogram in Fig. 2. The spectrogram shows the I/F spectra normalized at 2.227 $\mu$m and stacked together. The number of I/F spectra available for each observation is reported in Table 1. Europa's spectrogram appears highly uniform, showing

the intense water ice absorptions at 2 $\mu$m and at 2.8-2.9 $\mu$m on each spectrum. At wavelengths longer than 3 $\mu$m the I/F is in general noisier than at shorter wavelengths due to the intrinsic low reflectance of the surface and worse instrumental sensitivity.

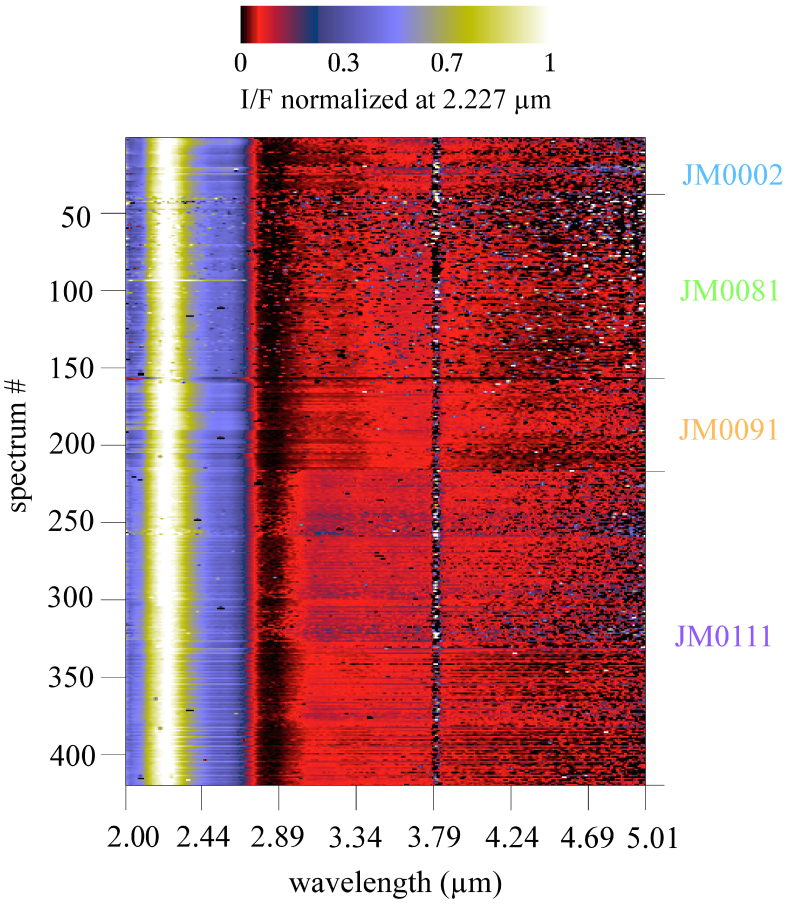


Figure 2: Europa's dataset spectrogram from JIRAM-SPE. Spectral axis is shown along the horizontal axis. The 419 observations listed in Table 1 are stacked along the vertical axis (observation number and Juno's orbits boundaries are shown on the left and right, respectively). The noise visible around 3.80 $\mu$m on all spectra is a residual caused by the instrumental order sorting filters junction. The I/F spectra shown in the next Fig. 3-central panel correspond to spectra #1-19 visible on the top of the spectrogram.

From the spectrogram is possible to retrieve single I/F spectra as horizontal profiles. As

an example, the median I/F of Europa derived from 19 spectra selected from the first session of the dataset (observation JM0002_160802_213108) is shown in Fig. 3-top panel. The single I/F spectra used to compute the median spectrum are reported in the central panel. The instrumental noise affecting JIRAM data is computed by comparing the measured spectral radiance with respect to the noise-equivalent spectral radiance (NESR). The NESR gives the minimum spectral radiance in W/(m$^2$ $\mu$m sr) corresponding to 1 DN as measured by the instrument at operative temperature conditions. The JIRAM NESR shown in Fig. 3-bottom panel is defined as:

$$NESR = \frac{STDEV(D(\lambda) + B(\lambda))}{Resp(\lambda)} \tag{3}$$

where $D(\lambda)$ is the dark current, $B(\lambda)$ is the background signal (equivalent to the sky) and $Resp(\lambda)$ is the instrument responsivity at wavelength ($\lambda$). These quantities are averages computed along the slit on all spatial samples. The determination of the instrument's responsivity is detailed in *Adriani et al.* (2017). The instrumental noise shown in Fig. 3 is computed from the ratio between Europa's median radiance and NESR. The noise on the I/F spectra is negligible between 2 and 2.7 $\mu$m where the Europa's flux is high and the instrument NESR is minimum. On the contrary, the noise progressively increases at longer wavelengths where Europa's flux is low and instrument sensitivity is worse.

A direct comparison of JIRAM and Galileo/NIMS data is complicated by the sparseness and spatial resolution of the available datasets. In Fig. 3-top panel we compare a JIRAM observation at high latitudes with a similar I/F spectrum by NIMS averaged above the north polar region (Hansen, G., personal communication, 2003). NIMS data are selected from Galileo's orbit G1 and include the north pole and bright limb (around lon=330°). Differently from JIRAM observations, NIMS data were acquired at lower phase angle (≈31°), with incidence angles varying from 4° to 84° and with emission angles from 3° to 84°. While the two spectra are remarkably similar between 2.227 and 2.7 $\mu$m, the 2 $\mu$m water ice band appears stronger in JIRAM than on NIMS spectrum. This could be a consequence of the different phase angle

between the two datasets (31° for NIMS, 90° for JIRAM) but we cannot exclude intrinsic differences between the composition of the two areas observed by JIRAM and NIMS since they do not match exactly. Both theoretical studies (*Hapke*, 1993; *Ciarniello et al.*, 2014) and observations of icy surfaces (*Filacchione et al.*, 2014, 2016a) have shown how the intensity of the infrared bands depends on phase angle. This is consequence of the fact that the efficiency of the multiple scattering, on which depends the intensity of the continuum level, is driven by phase angle and surface roughness. Conversely, the intensity of the absorption features is driven by the single scattering which is much less sensitive to illumination condition changes. From the theory of phase function described in *Gradie and Veverka* (1986) is known that the band depth decreases at low and at high phases, while it is almost constant across a wide range of phases, typically between 30°-40° and 100°-120° (depending on composition and grain size). In this range of phase angles the single scattering regime dominates throughout the entire absorption band. Conversely, at low phase angles (<30°-40°) the band depth decreases because the multiple scattering becomes predominant on the continuum, where albedo is higher but it is less effective at the band center where albedo is low and single scattering continue to prevail (*Hapke*, 1993). At high phase angles (>100°-120°), forward/multiple scattering prevails again on the continuum resulting in a significative decrease of the band depth. Due to the higher phase angle, JIRAM observations are therefore much less affected by multiple scattering than NIMS. Similar considerations are valid also to explain the higher I/F observed at longer wavelengths in the NIMS spectrum with respect to JIRAM's. Finally, a spectral shift of about 30 nm is seen between the two spectra: the position of the 2 $\mu$m band minimum, the peak at 2.227 $\mu$m and the feature at 2.541 $\mu$m appear shifted towards shorter wavelengths on NIMS spectrum. This shift is probably caused or by the low spectral sampling mode used in this specific NIMS observation or by a different nonice fraction between the two datasets.

Since single spectra are frequently marred by spikes caused by the harsh radiation environment and by the low SNR long wards 2.7 $\mu$m (see Fig. 3-central panel), we compute median

I/F spectra grouping all single spectra taken during the four orbits JM0002, JM0081, JM0091, JM0111 (Fig. 4). Taking advantage of the wide excursion in latitude covered by the JIRAM dataset (Fig. 1 and Table 1) during these orbits, different areas of Europa's surface can be compared among them by means of the following spectral characteristics:

1. the shape of the 2 $\mu$m water ice band around its minimum is broader on northern hemisphere (orbits JM0002 and JM0081) than of the southern hemisphere observations (orbits JM0081 and JM0111);
2. the intensity of the continuum level at 2.541 $\mu$m decreases moving from northern to southern hemisphere data. Also the sharpness of the inflection around 2.541 $\mu$m follows a similar trend;
3. the intensity of the 3.1 $\mu$m peak is fainter on the northern hemisphere data while becomes more intense on the southern hemisphere spectra;
4. conversely, the broad continuum peak at 3.5-3.6 $\mu$m is stronger than the 3.1 $\mu$m feature on spectra taken during orbits JM0002, JM0081 and JM0091 while it is less intense on JM0111 data;
5. JM0002 median I/F spectrum shows a faint absorption band centered at 3.5 $\mu$m compatible with a similar feature first detected by Galileo/NIMS (*Carlson et al.*, 1999a) and assigned to hydrogen peroxide ($H_2O_2$). However, this feature is not recognizable in the rest of the JIRAM dataset suggesting or a $H_2O_2$ distribution preferentially localized within the area observed during JM0002 (northern/antijovian hemisphere) or a spurious detection.

The implications of these spectral characteristics is discussed next.

## 5. Spectral Indicators

Starting from the characteristics and variability of the JIRAM spectral dataset we have discussed in the previous section, a set of six spectral indicators is employed to describe the

physical state and composition of Europa's surface. These indicators are the same previously used and validated for the analysis of Saturn's ice satellites and rings data acquired by VIMS on Cassini (*Filacchione et al.*, 2007, 2010, 2012, 2016a) and are applicable, with some precautions, also for Europa, water ice being one of the principal spectral endmembers:

1. 2 $\mu$m band center wavelength, $\lambda_{BC}$(2 $\mu$m), is used as a proxy of the water ice amorphous/crystalline state and of the non-ice material composition;
2. 2 $\mu$m band depth, BD(2 $\mu$m), is a proxy of water ice and non-ice material abundance, and regolith grain size distribution.
3. Ratio I/F(2.541 $\mu$m) / I/F(2.020 $\mu$m) is a proxy of the abundance of the non ice material;
4. Ratio I/F(3.100 $\mu$m) / I/F(2.847 $\mu$m) is another proxy of the surficial water ice amorphous/crystalline state;
5. Ratio I/F(3.630 $\mu$m) / I/F(2.227 $\mu$m) is a proxy of water ice grain size;
6. Wavelength of the I/F peak around 3.6 $\mu$m, $\lambda$(3.6 $\mu$m), is a proxy of water ice temperature.

The wavelengths used to define these indicators are marked in Fig. 3. Unfortunately, because the JIRAM spectral range starts from 2.0 $\mu$m, it is not possible to resolve the short-wavelength wing of the water ice band but only its minimum. As a consequence, we derive the $\lambda_{BC}$(2 $\mu$m) by fitting JIRAM data in the 2.0-2.2 $\mu$m with a $3^{rd}$-degree fit. The $I/F_{min}$ corresponding to the $\lambda_{BC}$(2 $\mu$m) is then used to compute the BD(2 $\mu$m) as

$$BD(2\ \mu m) = 1 - \frac{I/F_{min}}{I/F(2.227\ \mu m)} \tag{4}$$

We remark that the spectral indicators we are using are calibrated with respect to pure water ice grains. In presence of nonice materials mixed with water ice, both the absorption bands and continuum properties will change. For this reason in the following we are using the spectral indicators as "proxy" of water ice grain properties, water ice being the dominant endmember of Europa's surface and where water ice does not dominate, these proxies should be taken with caution. We are using a similar approach because JIRAM spectral range is limited in the 2-5

$\mu$m where is not possible to unambiguously retrieve nonice material composition. To achieve this it is necessary to explore Europa's surface with a more wide spectral range, including visible and near infrared wavelengths where diagnostic features are located, and with a much higher spatial resolution to better resolve nonice material endmembers. In the next sections a discussion of the results obtained from the analysis of the spectral indicators derived from each spectrum of the dataset is given.

## 6. Composition

The possibility of inferring Europa's surface composition is limited by JIRAM's 2-5 $\mu$m spectral range, which has been optimized to study Jupiter's atmosphere (*Adriani et al.*, 2018) and auroral emissions (*Mura et al.*, 2018). The lack of the VIS-NIR range makes JIRAM much less diagnostic of a comprehensive characterization of ice surface composition. Within these limits, JIRAM data are however valuable because they offer spatial coverage above both polar regions, albeit at coarse spatial resolution, which were largely unexplored by previous missions and are unaccessible from Earth-based observations. The JIRAM median I/F spectra (Fig. 3-4) are dominated by the presence of the intense 2.0 and 3.0 $\mu$m water ice bands. The water ice Fresnel's peak at 3.1 $\mu$m appears to be low-contrast across the entire dataset. JIRAM spectra show similarities with synthetic spectra of water ice simulated by means of *Hapke* (1993) theory following the method described in *Raponi et al.* (2016). The spectral simulations are performed using crystalline water ice optical constants measured at 130 K (*Mastrapa et al.*, 2008, 2009) assuming a phase function p(g)=0.5 (*Clark et al.*, 2012) and a phase angle g=90° in order to match JIRAM observational conditions. The resulting reflectance spectra for nine grain sizes between 10 $\mu$m and 1 cm are shown in Fig. 5-left panel. Laboratory reflectance spectra of three frozen eutectic chlorine salts ($MgCl_2$, NaCl, KCl) measured at T=-30°C (*Hanley et al.*, 2014) are reported for comparison in Fig. 5-right panel. *Shirley et al.* (2010) have retrieved the surface composition of different units finding that ridged plains are compatible with ternary mixtures

of water ice (46%), hydrated sulfuric acid (27%) and hydrated salts (27%) while smooth low albedo plains are made of hydrated salts (62%), hydrated sulfuric acid (27%) and water ice (10%).

Apart from the variability caused by the grain size, that we will discuss in the next section, pure water ice is not able to fully reproduce Europa's data: this is particularly evident when comparing the intensity of the reflectance in the 2 $\mu$m band absorption with the inflection of the continuum at 2.5 $\mu$m. Other than large cm-sized grains, the ratio I/F(2.541 $\mu$m) / I/F(2.020 $\mu$m) is always positive and much larger than 1 on water ice synthetic spectra (Fig. 5-left panel). This is the typical case observed in Saturn's ice satellites and rings spectra (*Filacchione et al.*, 2012) where water ice is the dominant endmember. Conversely, in Europa spectra this ratio is systematically lower and distributed with an average value of about 1 in the JIRAM dataset (Fig. 6). To reproduce a similar behavior it is necessary to introduce additional endmembers, such as chlorinated salts, hydrated sulfates, sulfate brines, and hydrated sulfuric acid, which are able to reduce the reflectance at 2.5 $\mu$m to the same value of the 2 $\mu$m band (Fig. 5-right panel).

Moving from orbit JM0002 to JM0111 a decreasing trend is observed in the ratio series: observations acquired in the northern hemisphere and equatorial areas during orbits JM0002 (blue points) and JM0081 (green) are those with the larger ratio value ($\approx$1.15 to 1.25), indicating a lower abundance of contaminant. The maximum amount of contaminant is measured across the southern hemisphere and equatorial region observed during orbits JM0091 (orange) and #11 (magenta sector) where the average ratio is $\approx$1.

## 7. Grain size

The dimension of pure water ice regolith grains can be derived from the measurement of the I/F(3.630 $\mu$m) / I/F(2.227 $\mu$m) ratio and from the BD(2 $\mu$m). The values of these spectral indicators as a function of the grain size is calibrated starting from the synthetic water ice

| Grain size | $\frac{I/F(3.630\ \mu m)}{I/F(2.227\ \mu m)}$ | BD(2 $\mu$m) |
|---|---|---|
| 10 $\mu$m | 0.31 | 0.50 |
| 30 $\mu$m | 0.15 | 0.69 |
| 50 $\mu$m | 0.10 | 0.77 |
| 80 $\mu$m | 0.07 | 0.84 |
| 100 $\mu$m | 0.05 | 0.86 |
| 200 $\mu$m | 0.03 | 0.93 |
| 0.2 cm | 0.15 | 0.90 |
| 0.5 cm | 0.54 | 0.64 |

Table 2: Reference values of I/F(3.630 $\mu$m) / I/F(2.227 $\mu$m) ratio and BD(2 $\mu$m) as function of grain size for water ice. Values are derived from synthetic spectra computed at phase 90° and temperature T=130 K shown in Fig. 5-left panel.

spectra shown in Fig. 5-left panel and tabulated in Table 2.

As shown in Fig. 7-top panel, the I/F(3.630 $\mu$m) / I/F(2.227 $\mu$m) ratio is almost constant across the entire JIRAM dataset and is dispersed with a median value of 0.079 which, according to Table 2, is compatible with grain sizes of 50-80 $\mu$m and ≈0.5 cm. The BD(2 $\mu$m) distribution (Fig. 7-bottom panel) shows a small decrease moving from northern to southern latitudes, which could indicate a prevalence of smaller grains on the latter. The dataset has a median value of 0.60 which is compatible with small 10-30 $\mu$m or large 0.5 cm grain sizes.

The I/F(3.630 $\mu$m) / I/F(2.227 $\mu$m) ratio and BD(2 $\mu$m) values we have measured on the JIRAM dataset are compatible with both tens of microns and fraction of centimeter grains sizes. A similar degeneracy is due to the trend characterizing the two indicators as a function of the grain size (Fig. 8-left panel). Theoretical points are in fact aligned along two parallel branches converging on the inversion point placed at BD(2 $\mu$m)=0.93 that corresponds to 200 $\mu$m grain size. Two almost parallel branches describe the small (tens to hundred of microns) and large (fraction of centimeter) grains at lower band depths: the former are placed along

lower I/F(3.630 $\mu$m) / I/F(2.227 $\mu$m) ratio values, the latter at higher values. The majority of JIRAM data (Fig. 8-right panel) are distributed along the lower branch pointing to small (<200 $\mu$m) grain sizes, but a fraction of them is along the upper branch, which implies compatibility with large (>200 $\mu$m) grain sizes.

Thanks to the availability of two spectral indicators which rely on the properties of the scattering of the continuum (the I/F(3.630 $\mu$m) / I/F(2.227 $\mu$m) ratio) and on the strength of the absorption (the 2 $\mu$m band depth), we can conclude that the size distribution on the surface of Europa is dominated by grains tens to hundreds of microns in size with a possible smaller fraction of millimeters size grains.

We need to interpret these results with caution: on the one hand the presence of non ice materials can significantly change the values of the spectral indicators which in our analysis are based on pure water ice composition. The fact that both indicators converge on similar grain size values is a significant result, showing that the nonice material is not influencing too much the water ice reflectance at these wavelengths. On the contrary, the presence of millimeter-sized grains, while compatible with the spectral indicators, appears to be inconsistent with the properties of the synthetic spectra shown in Fig. 5 which are characterized by an intense saturation of the 2 $\mu$m band and by low levels of continuum. Similar properties are not seen in the average spectra of Europa.

## 8. Water ice amorphization

The environmental conditions necessary to maintain water ice in both crystalline and amorphous states exist on the surface of Europa: the amorphous phase is produced from radiolysis of crystalline ice by high energy electrons and ions from Jupiter's magnetosphere (*Carlson et al.*, 2009) and from condensation of sublimated and sputtered molecules (*Baragiola*, 2003). As reported in *Nordheim et al.* (2018), the areas of the surface more altered by radiation are those located within the two equatorial "lenses" centered on the apex of the leading and trailing hemi-

spheres and extending in latitude up to about ±40°. According to these simulations, along the jovian meridian the two radiation lenses have the lower extension in latitude, about ±15° from equator. This is the region mainly observed by JIRAM, especially during orbits JM0091 and JM0111. We would expect, therefore, a prevalence of the amorphous phase in the equatorial regions rather than on the polar areas where the crystalline form would be more abundant. In the infrared range sensed by JIRAM, the two water ice forms can be recognized by measuring the position of the 2 $\mu$m band center and the relative intensity of the 3.1 $\mu$m Fresnel peak. As laboratory measurements by *Leto et al.* (2005) and *Mastrapa et al.* (2008) have shown, the center of the 2.0 $\mu$m absorption band is strongly influenced by the amorphous and crystalline phases. While for crystalline ice the center of the $\lambda_{BC}$(2 $\mu$m) is temperature-dependent, shifting from 2.02 $\mu$m at T=20 K to 2.05 $\mu$m at T=155K (*Grundy and Schmitt*, 1998), for the amorphous phase $\lambda_{BC}$(2 $\mu$m) = 2.00 $\mu$m independent of temperature. Within the limit of the JIRAM spectral range, we compute the $\lambda_{BC}$(2 $\mu$m) by fitting JIRAM data in the 2.0-2.2 $\mu$m range with a $3^{rd}$-degree fit. The resulting distribution of the $\lambda_{BC}$(2 $\mu$m) indicator is shown in Fig. 9-top panel. The distribution of the measurements has a median value of 2.05 $\mu$m on JM0002 data and 2.04 $\mu$m on JM0081, JM0091 and JM0111 orbits datasets. For pure water ice composition this corresponds to a prevalence of the crystalline form in the northern/antijovian hemisphere (JM002) and a larger presence of amorphous form in the northern/jovian (JM0081) and in the southern/jovian hemisphere regions (JM0091 and JM0111 orbits) in agreement with the analysis of telescopic spectral data performed by *Ligier et al.* (2016). These results partially match with the presence of amorphous water ice across the equatorial region as predicted by magnetospheric models: the majority of observations with the shortest $\lambda_{BC}$(2 $\mu$m) occur in orbit JM0111, where JIRAM has observed the south-equator region along the jovian meridian. As discussed in section 2, at 2 $\mu$m photons can penetrate the ice down to about 10 cm and for this reason the $\lambda_{BC}$(2 $\mu$m) is sensitive to the ice form within this depth. In order to better evaluate the amorphization of the surface it is possible to use the ratio I/F(3.100 $\mu$m)

/ I/F(2.847 $\mu$m) as a further proxy. At 3.1 $\mu$m the water ice acts like a reflector and the photons are probing a very shallow (submicron) layer of the surface. The ratio measures the intensity of the 3.1 $\mu$m Fresnel's peak with respect to the maximum absorption at 2.847 $\mu$m. As laboratory studies have demonstrated, the intensity of the Fresnel's peak is much higher on crystalline water ice than on amorphous ice (*Mastrapa et al.*, 2009). A qualitative analysis of the JIRAM data distribution, shown in Fig. 9-bottom panel, evidences that the ratio increases from a median value of 3.8 in JM0002 orbit data to 4.5 in JM0081, to 5.6 in JM0091, to 7.1 in JM0111. The maximum amorphization on the surface, as indicated by the lower ratio values, is therefore observed on the northern hemisphere.

## 9. Temperature

The last spectral indicator we have measured is the wavelength of the I/F peak around 3.6 $\mu$m, $\lambda$(3.6 $\mu$m), which in pure water ice depends on the temperature of the sample. This technique has been used to retrieve diurnal temperatures of Saturn's ice satellites (*Filacchione et al.*, 2016a) and rings (*Filacchione et al.*, 2014). When water ice cools down the minimum of the imaginary index k at about 3.6 $\mu$m shifts towards shorter wavelengths (*Mastrapa et al.*, 2009). Laboratory measurements on small water ice grains observed under standard illumination conditions (phase 30°) by *Clark et al.* (2012) have shown that the 3.6 $\mu$m reflectance peak shifts in wavelength from 3.675 $\mu$m for a sample temperature of T=172 K to 3.58 $\mu$m at T=88 K. This corresponds to a spectral shift of about 90 nm (10 JIRAM spectral bands) in the 3.6 $\mu$m continuum peak feature. At intermediate temperatures, T=123 K and T=131 K, the peak's wavelength is placed at 3.62 $\mu$m and 3.65 $\mu$m, respectively. We compute the $\lambda$(3.6 $\mu$m) as the wavelength of the maximum I/F fitted by means of a $2^{nd}$-degree fit in the 3.3-4.0 $\mu$m spectral range. The bands corresponding to the position of the instrumental order sorting filter at about 3.8 $\mu$m have been filtered out. Despite the low signal to noise ratio in this spectral range, which causes a large dispersion in the fitted data, JIRAM data are dispersed around a

median value of 3.573 $\mu$m which corresponds to diurnal temperature of 88 K. This is the average temperature retrieved from observations taken along terminator ($\approx 90^\circ$ phase angle, see Table 1). Averaging the observations during the four single orbits (Fig. 4), this method gives peak positions of 3.620 $\mu$m or $\approx$124 K on JM0002 (northern/antijovian hemisphere), 3.586 $\mu$m or $\approx$89 K on JM0081 (northern/jovian hemisphere), 3.643 $\mu$m or $\approx$132 K on JM0091 and 3.537 $\mu$m or <<88 K on JM0111 (both on southern/jovian hemisphere). This variability is probably the result of the different spatial resolution of JIRAM observations along the four orbits (see Fig. 1). Noteworthy, the range of temperature retrieved by JIRAM (<<88 K to 132 K) is in good agreement with previous results by *Spencer et al.* (1999). Finally, since this method is valid for reflectance data it can be used only to retrieve diurnal temperatures.

## 10. Conclusions

Spectral indicators applied to JIRAM data have permitted inference of information about composition, regolith grain size, water ice form and temperature across broad swaths of Europa's surface. The surface composition appears dominated by water ice contaminated by the presence of non-ice endmembers, like hydrated salts and acid-rich compounds, necessary to equalize the ratio of the I/F within the 2 $\mu$m band to the 2.5 $\mu$m continuum. Purer water ice is observed by JIRAM on the northern hemisphere than on the southern along the jovian meridian. Water ice appears in both crystalline and amorphous forms: a prevalence of the first is obtained from the 2 $\mu$m band center wavelength on the northern hemisphere while the latter prevails when analyzing the properties of the 3.1 $\mu$m Fresnel peak. This result further evidences the different skin depth at which radiation is efficient in water ice amorphization. The surface regolith grain size distribution encompasses tens to hundred of microns sizes with a possible tail towards larger grains suggesting possible water ice grain mobilization, aggregation and sintering. These processes cannot be excluded since the diurnal maximum temperature, derived from the 3.6 $\mu$m continuum properties, is 132 K and it is high enough to activate them.

Our analyses are performed through spectral indicators calibrated on water ice composition and do not take into account the presence of nonice materials. To better constrain the nature of these contaminants and disentangle their influence on water ice grain properties is necessary to measure the spectral reflectance at wavelengths shorter than 2 $\mu$m, a range precluded to JIRAM, where diagnostic spectral features of nonice materials are located. Before the end of the Juno mission other possibilities to observe the surface of Europa will occur. The JIRAM team will exploit them to continue to acquire infrared spectra and images of the surface necessary to enlarge the dataset and improve the spatial coverage and resolution. These infrared observations will be the last acquired by a spacecraft before the future ESA's Juice and NASA's EuropaClipper missions currently scheduled after year 2030.

## Acknowledgments

The authors acknowledge the financial support from Italian Space Agency (ASI) for the Juno-JIRAM program through ASI-INAF agreement number 2016-23-H.0 and for the US authors, NASA. This research has made use of NASA's Astrophysics Data System. All data used in this work are publicly available through NASA-PDS.

## References

Acton, C. (1996). Ancillary data services of NASA's Navigation and Ancillary Information Facility. *Planetary and Space Science*, 44, 65-70.

Adriani, A., Filacchione, G., Di Iorio, T., Turrini, D., Noschese, R., Cicchetti, A., Grassi, D., Mura, A., Sindoni, G., Zambelli, M., Piccioni, G., Capria, M. T., Tosi, F., Orosei, R., Dinelli, B. M., Moriconi, M. L., Roncon, E., Lunine, J. I., Becker, H. N., Bini, A., Barbis, A., Calamai, L., Pasqui, C., Nencioni, S., Rossi, M., Lastri, M., Formaro, R., Olivieri, A., (2017). JIRAM, the Jovian Infrared Auroral Mapper. *Space Science Reviews*, 213, 393-446.

567 Adriani, A., Mura, A., Orton, G., Hansen, C., Altieri, F., Moriconi, M. L., Rogers, J., Eichstädt,
568 G., Momary, T., Ingersoll, A. P., Filacchione, G., Sindoni, G., Tabataba-Vakili, F., Dinelli,
569 B. M., Fabiano, F., Bolton, S. J., Connerney, J. E. P., Atreya, S. K., Lunine, J. I., Tosi, F.,
570 Migliorini, A., Grassi, D., Piccioni, G., Noschese, R., Cicchetti, A., Plainaki, C., Olivieri, A.,
571 O'Neill, M. E., Turrini, D., Stefani, S., Sordini, R., Amoroso, M., (2018), Clusters of cyclones
572 encircling Jupiter's poles, *Science*, 555, 216-219.

573 Baragiola, R. A., (2003). Water ice on outer solar system surfaces: Basic properties and radia-
574 tion effects, *Planetary Space Science*, 51, 953-961.

575 Blaney, D. L., Clark, R. N., Dalton, J. B., Davies, A. G., Green, R. O., Hibbits, C. A., Langevin,
576 Y., Lunine, J. I., McCord, T. B., Paranicas, C., Murchie, S. L., Seelos, F. P., Soderblom,
577 J. M., (2017). The Mapping Imaging Spectrometer for Europa (MISE) Investigation: Ex-
578 ploring Europa's Habitability Using Compositional Mapping, *Lunar and Planetary Science*
579 *Conference*, 48, 2244.

580 Bolton, S. J., Connerney, J. E. P., (2017). Editorial: Topical Collection of the Juno Mission
581 Science Objectives, Instruments, and Implementation, *Space Science Reviews*, 213, 1-3.

582 Brown, R. H., Baines, K. H., Bellucci, G., Bibring, J.-P., Buratti, B. J., Capaccioni, F., Cerroni,
583 P., Clark, R. N., Coradini, A., Cruikshank, D. P., Drossart, P., Formisano, V., Jaumann, R.,
584 Langevin, Y., Matson, D. L., McCord, T. B., Mennella, V., Nelson, R. M., Nicholson, P. D.,
585 Sicardy, B., Sotin, C., Amici, S., Chamberlain, M. A., Filacchione, G., Hansen, G., Hibbitts,
586 K., Showalter, M., (2003). Observations with the Visual and Infrared Mapping Spectrometer
587 (VIMS) during Cassini's flyby of Jupiter, *Icarus*, 164, 461-470.

588 Brown, R. H., Baines, K. H., Bellucci, G., Bibring, J.-P., Buratti, B. J., Capaccioni, F., Cerroni,
589 P., Clark, R. N., Coradini, A., Cruikshank, D. P., Drossart, P., Formisano, V., Jaumann,
590 R., Langevin, Y., Matson, D. L., McCord, T. B., Mennella, V., Miller, E., Nelson, R. M.,

591 Nicholson, P. D., Sicardy, B., Sotin, C., (2004). The Cassini Visual And Infrared Mapping
592 Spectrometer (Vims) Investigation. *Space Science Reviews*, 115, 111-168.

593 Buratti, B., Veverka, J., (1983). Voyager Photometry of Europa, *Icarus*, 55, 93-110.

594 Carlson, R. W., Weissman, P. R., Smythe, W. D., Mahoney, J. C., (1992). Near-Infrared
595 Mapping Spectrometer experiment on Galileo, *Space Science Reviews*, 60, 457-502.

596 Carlson, R. W., Anderson, M. S., Johnson, R. E., Smythe, W. D., Hendrix, A. R., Barth,
597 C. A., Soderblom, L. A., Hansen, G. B., McCord, T. B., Dalton, J. B., Clark, R. N., Shirley,
598 J. H., Ocampo, A. C., Matson, D. L., (1999a). Hydrogen Peroxide on the Surface of Europa,
599 *Science*, 283, 2062.

600 Carlson, R. W., Johnson, R. E., Anderson, M. S. (1999b). Sulfuric acid on Europa and the
601 radiolytic sulfur cycle, *Science*, 286, 97-99.

602 Carlson, R. W., Anderson, M. S., Johnson, R. E., Schulman, M. B., Yavrouian, A. H. (2002).
603 Sulfuric Acid Production on Europa: The Radiolysis of Sulfur in Water Ice, *Icarus*, 157,
604 456-463.

605 Carlson, R. W., Anderson, M. S., Mehlman, R., Johnson, R. E., (2005). Distribution of hydrate
606 on Europa: Further evidence for sulfuric acid hydrate, *Icarus*, 177, 461-471.

607 Carlson, R. W., Calvin, W. M., Dalton, J. B., Hansen, G. B., Hudson, R. L., Johnson, R. E.,
608 McCord, T. B., Moore, M. H., (2009). Europa's Surface Composition, in *Europa*, Edited by
609 Robert T. Pappalardo, William B. McKinnon, Krishan K. Khurana, University of Arizona
610 Press, Tucson, p.283.

611 Ciarniello, M., Capaccioni, F., Filacchione, G., Clark, R. N., Cruikshank, D. P., Cerroni, P.,
612 Coradini, A., Brown, R. H., Buratti, B. J., Tosi, F., Stephan, K., (2011). Hapke modeling of
613 Rhea surface properties through Cassini-VIMS spectra, *Icarus*, 214, 541-555.

614 Ciarniello, M., Capaccioni, F., Filacchione, G., (2014). A test of Hapke's model by means of
615 Monte Carlo ray-tracing, *Icarus*, 237, 293-305.

616 Clark, R. N., Cruikshank, D. P., Jaumann, R., Brown, R. H., Stephan, K., Dalle Ore, C. M.,
617 Eric Livo, K., Pearson, N., Curchin, J. M., Hoefen, T. M., Buratti, B. J., Filacchione, G.,
618 Baines, K. H., Nicholson, P. D., (2012). The surface composition of Iapetus: Mapping results
619 from Cassini VIMS, *Icarus*, 218, 831-860.

620 Dalton, J. B., Prieto-Ballesteros, O., Kargel, J. S., Jamieson, C. S., Jolivet, J., Quinn, R.
621 (2005). Spectral comparison of heavily hydrated salts with disrupted terrains on Europa,
622 *Icarus*, 177, 472-490.

623 Dalton, J. B., Shirley, J. H., Kamp, L. W,., (2012). Europa's icy bright plains and dark linea:
624 Exogenic and endogenic contributions to composition and surface properties. *Journal of Geo-*
625 *physical Research: Planets*, 117(E03003).

626 Fanale, F. P., Granahan, J. C., McCord, T. B., Hansen, G., Hibbitts, C. A., Carlson, R.,
627 Matson, D., Ocampo, A., Kamp, L., Smythe, W., Leader, F., Mehlman, R., Greeley, R.,
628 Sullivan, R., Geissler, P., Barth, C., Hendrix, A., Clark, B., Helfenstein, P., Veverka, J.,
629 Belton, M. J. S., Becker, K., Becker, T., Galileo NIMS, UVS instrument Teams, (1999).
630 Galileo's Multiinstrument Spectral View of Europa's Surface Composition, *Icarus*, 139, 179-
631 188.

632 Fanale, F. P., Li, Y.-H., De Carlo, E., Farley, C., Sharma, S. K., Horton, K., Granahan, J. C.,
633 (2001). An experimental estimate of Europa's "ocean" composition-independent of Galileo
634 orbital remote sensing, *JGR*, 106, 14595-14600.

635 Filacchione, G., Ammannito, E., Coradini, A., Capaccioni, F., Piccioni, G., de Sanctis, M. C.,
636 Dami, M., Barbis, A., (2006). On-ground characterization of Rosetta/VIRTIS-M. II. Spatial
637 and radiometric calibrations, *Review of Scientific Instruments*, 77, 103106-103106.

638 Filacchione, G., Capaccioni, F., McCord, T. B., Coradini, A., Cerroni, P., Bellucci, G., Tosi,
639 F., D'Aversa, E., Formisano, V., Brown, R. H., Baines, K. H., Bibring, J. P., Buratti, B. J.,
640 Clark, R. N., Combes, M., Cruikshank, D. P., Drossart, P., Jaumann, R., Langevin, Y.,
641 Matson, D. L., Mennella, V., Nelson, R. M., Nicholson, P. D., Sicardy, B., Sotin, C., Hansen,
642 G., Hibbitts, K., Showalter, M., Newman, S. (2007). Saturn's icy satellites investigated by
643 Cassini-VIMS. I. Full-disk properties: 350-5100 nm reflectance spectra and phase curves.
644 *Icarus*, 186, 259-290.

645 Filacchione, G., Capaccioni, F., Clark, R. N., Cuzzi, J. N., Cruikshank, D. P., Coradini, A.,
646 Cerroni, P., Nicholson, P. D., McCord, T. B., Brown, R. H., Buratti, B. J., Tosi, F., Nelson,
647 R. M., Jaumann, R., Stephan, K., (2010). Saturn's icy satellites investigated by Cassini-
648 VIMS. II. Results at the end of nominal mission, *Icarus*, 206, 507-523.

649 Filacchione, G., Capaccioni, F., Ciarniello, M., Clark, R. N., Cuzzi, J. N., Nicholson, P. D.,
650 Cruikshank, D. P., Hedman, M. M., Buratti, B. J., Lunine, J. I., Soderblom, L. A., Tosi,
651 F., Cerroni, P., Brown, R. H., McCord, T. B., Jaumann, R., Stephan, K., Baines, K. H.,
652 Flamini, E. (2012). Saturn's icy satellites and rings investigated by Cassini-VIMS: III - Radial
653 compositional variability. *Icarus*, 220, 1064-1096.

654 Filacchione, G., Ciarniello, M., Capaccioni, F., Clark, R. N., Nicholson, P. D., Hedman, M. M.,
655 Cuzzi, J. N., Cruikshank, D. P., Dalle Ore, C. M., Brown, R. H., Cerroni, P., Altobelli,
656 N., Spilker, L. J., (2014). Cassini-VIMS observations of Saturn's main rings: I. Spectral
657 properties and temperature radial profiles variability with phase angle and elevation, *Icarus*,
658 241, 45-65.

659 Filacchione, G., D'Aversa, E., Capaccioni, F., Clark, R. N., Cruikshank, D. P. Ciarniello, M.,
660 Cerroni, P., Bellucci, G., Brown, R. H., Buratti, B. J., Nicholson, P. D., Jaumann, R.,
661 McCord, T. B., Sotin, C., Stephan, K., Dalle Ore, C. M. (2016a). Saturn's icy satellites
662 investigated by Cassini-VIMS. IV. Daytime temperature maps, *Icarus*, 271, 292-313.

663 Filacchione, G., de Sanctis, M. C., Capaccioni, F., Raponi, A., Tosi, F., Ciarniello, M., Cerroni,
664 P., Piccioni, G., Capria, M. T., Palomba, E., Bellucci, G., Erard, S., Bockelee-Morvan, D.,
665 Leyrat, C., Arnold, G., Barucci, M. A., Fulchignoni, M., Schmitt, B., Quirico, E., Jaumann,
666 R., Stephan, K., Longobardo, A., Mennella, V., Migliorini, A., Ammannito, E., Benkhoff, J.,
667 Bibring, J. P., Blanco, A., Blecka, M. I., Carlson, R., Carsenty, U., Colangeli, L., Combes,
668 M., Combi, M., Crovisier, J., Drossart, P., Encrenaz, T., Federico, C., Fink, U., Fonti, S.,
669 Ip, W. H., Irwin, P., Kuehrt, E., Langevin, Y., Magni, G., McCord, T., Moroz, L., Mottola,
670 S., Orofino, V., Schade, U., Taylor, F., Tiphene, D., Tozzi, G. P., Beck, P., Biver, N., Bonal,
671 L., Combe, J.-P., Despan, D., Flamini, E., Formisano, M., Fornasier, S., Frigeri, A., Grassi,
672 D., Gudipati, M. S., Kappel, D., Mancarella, F., Markus, K., Merlin, F., Orosei, R., Rinaldi,
673 G., Cartacci, M., Cicchetti, A., Giuppi, S., Hello, Y., Henry, F., Jacquinod, S., Reess, J. M.,
674 Noschese, R., Politi, R., Peter, G., (2016b). Exposed water ice on the nucleus of comet
675 67P/Churyumov-Gerasimenko, *Nature*, 529, 368-372.

676 Gradie, J., Veverka, J., (1986). The wavelength dependence of phase coefficients, *Icarus*, 66,
677 455?467.

678 Greenberg, R. (2005), *Europa, The Ocean Moon: Search for an Alien Biosphere*, Springer +
679 Praxis Books.

680 Grundy, W. M., Schmitt, B., (1998). The temperature-dependent near-infrared absorption
681 spectrum of hexagonal $H_2O$ ice, *Journal of Geophysical Research*, 103, 25809-25822.

682 Grundy, W. M., Buratti, B. J., Cheng, A. F., Emery, J. P., Lunsford, A., McKinnon, W. B.,
683 Moore, J. M., Newman, S. F., Olkin, C. B., Reuter, D. C., Schenk, P. M., Spencer, J. R.,
684 Stern, S. A., Throop, H. B., Weaver, H. A., (2007). New Horizons Mapping of Europa and
685 Ganymede, *Science*, 318, 234-237.

686 Gundlach, B., Ratte, J., Blum, J., Oesert, J., Gorb, S. N., (2018). Sintering and sublimation

of micrometre-sized water-ice particles: the formation of surface crusts on icy Solar System bodies, *Monthly Notices of the Royal Astronomical Society*, 479, 5272-5287.

Hagen, W., Tielens, A. G. G. M., Greenberg, J. M. (1981). The infrared spectra of amorphous solid water and ice Ic between 10 and 140 K, *Chem. Phys.*, 56, 367-379.

Hand, K. P., Chyba, C. F., (2007). Empirical constraints on the salinity of the europan ocean and implications for a thin ice shell, *Icarus*, 189, 424-438.

Hanley, J., Dalton, J. B., Chevrier, V. F., Jamieson, C. S., Barrows, R. S., (2014). Reflectance spectra of hydrated chlorine salts: The effect of temperature with implications for Europa, *Journal of Geophysical Research (Planets)*, 119, 2370-2377.

Hansen, G. B., McCord, T., (2004). Amorphous and crystalline ice on the Galilean satellites: A balance between thermal and radiolytic processes, *Journal of Geophysical Research*, 109(E1).

Hansen, G. B., McCord, T., (2008). Widespread CO_2and other non-ice compounds on the anti-Jovian and trailing sides of Europa from Galileo/NIMS observations, *Geophys. Res. Lett.* 35, L01202.

Hansen, G. B., (2009), Calculation of single-scattering albedos: Comparison of Mie results with Hapke approximations, *Icarus*, 203, 672-676.

Hapke, B., (1993). *Theory of Reflectance and Emittance Spectroscopy*, Cambridge Univ. Press, Cambridge, UK.

Häßner, D., Mutschke, H., Blum, J., Zeller, T., Gundlach, B., (2018). Laboratory measurements of the sub-millimeter opacity of amorphous and micro-particulate $H_2O$ ices for temperatures above 80 K, *Monthly Notices of the Royal Astronomical Society*, doi = 10.1093/mnras/sty2664.

709 Jenniskens, P., Blake, D. F., Kouchi, A., (1998). Amorphous Water Ice: a Solar System Mate-
710 rial, *Solar System Ices*, Astrophysics and Space Science Library, 227, Schmitt, B. , de Bergh,
711 C., Festou, M. editors, page, 139.

712 Kurucz R. L., (1994), in Rabin D. M., Jefferies J. T., Lindsey C. eds, Proc. IAU Symp. 154,
713 Infrared Solar Physics, Kluwer, Dordrecht, p. 523.

714 Langevin, Y., Piccioni, G., Eng, P., Filacchione, G., Poulet, F. and Majis Team, (2014). The
715 MAJIS VIS-NIR Imaging Spectrometer for the JUICE Mission, *Lunar and Planetary Science*
716 *Conference*, 45, 2493.

717 Leto, G., Baratta, G. A., (2003). Ly-alpha photon induced amorphization of Ic water ice at
718 16 Kelvin. Effects and quantitative comparison with ion irradiation, *Astronomy and Astro-*
719 *physics*, 397, 7-13.

720 Leto, G., Gomis, O., Strazzulla, G., (2005). The reflectance spectrum of water ice: Is the 1.65
721 $\mu$m peak a good temperature probe? *Mem. Soc. Astron. Ital.* 6 (Suppl.), 57-62.

722 Ligier, N., Poulet, F., Carter, J., Brunetto, R., Gourgeot, F. (2016). VLT/SINFONI Obser-
723 vations of Europa: New Insights into the Surface Composition, *The Astronomical Journal*,
724 151(6), 163.

725 Lynch, D. K. (2005), The Infrared spectral signature of water ice in the vacuum cryogenic
726 AI&T environment, *The Aerospace Corporation report*, NO. TR-2006(8570)-1.

727 Mastrapa, R. M. E., Brown, R. H., (2006). Ion irradiation of crystalline H $_2$O-ice: Effect on
728 the 1.65-$\mu$m band, *Icarus*, 183, 207-214.

729 Mastrapa, R.M., Bernstein, M.P., Sandford, S.A., Roush, T.L., Cruikshank, D.P., Dalle Ore,
730 C.M., (2008). Optical constants of amorphous and crystalline $H_2O$-ice in the near infrared
731 from 1.1 to 2.6 $\mu$m, *Icarus*, 197, 307-320.

732 Mastrapa, R.M., Sandford, S.A., Roush, T.L., et al., (2009). Optical constants of amorphous
733 and crystalline $H_2O$-ice: 2.5 - 22 $\mu$m (4000 - 455 $cm^{-1}$) optical constants of $H_2O$-ice, *Astro-*
734 *physical Journal*, 701, 1347-1356.

735 McCord, T. B., Hansen, G. B., Fanale, F. P., Carlson, R. W., Matson, D. L., Johnson, T. V.,
736 Smythe, W. D., Crowley, J. K., Martin, P. D., Ocampo, A., Hibbitts, C. A., Granahan, J. C.,
737 (1998). Salts on Europa's Surface Detected by Galileo's Near Infrared Mapping Spectrometer,
738 *Science*, 280, 1242.

739 McCord, T. B., Hansen, G. B., Matson, D. L., Jonhson, T. V., Crowley, J. K., Fanale, F. P.,
740 Carlson, R. W., Smythe, W. D., Martin, P. D., Hibbitts, C. A., Granahan, J. C., Ocampo, A.,
741 (1999). Hydrated salt minerals on Europa's surface from the Galileo near-infrared mapping
742 spectrometer (NIMS) investigation, *JGR*, 104, 11827-11852.

743 McCord, T. B., Coradini, A., Hibbitts, C. A., Capaccioni, F., Hansen, G. B., Filacchione, G.,
744 Clark, R. N., Cerroni, P., Brown, R. H., Baines, K. H., Bellucci, G., Bibring, J.-P., Buratti,
745 B. J., Bussoletti, E., Combes, M., Cruikshank, D. P., Drossart, P., Formisano, V., Jaumann,
746 R., Langevin, Y., Matson, D. L., Nelson, R. M., Nicholson, P. D., Sicardy, B., Sotin, C.,
747 (2004). Cassini VIMS observations of the Galilean satellites including the VIMS calibration
748 procedure, *Icarus*, 172, 104-126.

749 Moore, M. H., Hudson, R. L., (1992). Far-infrared spectral studies of phase changes in water
750 ice induced by proton irradiation, *Astrophysical Journal*, 401, 353-360.

751 Mura, A., Adriani, A., Connerney, J. E. P., Bolton, S., Altieri, F., Bagenal, F., Bonfond, B.,
752 Dinelli, B. M., Gérard, J.-C., Greathouse, T., Grodent, D., Levin, S., Mauk, B., Moriconi,
753 M. L., Saur, J., Waite, J. H., Amoroso, M., Cicchetti, A., Fabiano, F., Filacchione, G.,
754 Grassi, D., Migliorini, A., Noschese, R., Olivieri, A., Piccioni, G., Plainaki, C., Sindoni, G.,

Sordini, R., Tosi, F., Turrini, D., (2018). Juno observations of spot structures and a split tail in Io-induced aurorae on Jupiter, *Science*, 361, 774-777.

Nordheim, T. A., Hand, K. P., Paranicas, C., (2018). Preservation of potential biosignatures in the shallow subsurface of Europa, *Nature Astronomy*, 2, 673-679.

Noschese, R., Cicchetti, A., Sordini, R., Cartacci, M., Brooks, S., Lastri, M., Adriani, A., Mura, A., Filacchione, G., Becker, H., Bini, A., Pasqui, C., Migliorini, A., Moriconi, M. L., Grassi, D., Altieri, F., Dinelli, B. M., Piccioni, G., Tosi, F., Turrini, D., Sindoni, G., Olivieri, A., Plainaki, C., (under review). Juno/JIRAM: Planning and Commanding activities, *Advances in Space Research*.

Poch, O., Cerubini, R., Pommerol, A., Jost, B., Thomas, N., (2018). Polarimetry of Water Ice Particles Providing Insights on Grain Size and Degree of Sintering on Icy Planetary Surfaces, *Journal of Geophysical Research*, 123, Issue 10, 2564-2584.

Porco, C. C., Helfenstein, P., Thomas, P. C., Ingersoll, A. P., Wisdom, J., West, R., Neukum, G., Denk, T., Wagner, R., Roatsch, T., Kieffer, S., Turtle, E., McEwen, A., Johnson, T. V., Rathbun, J., Veverka, J., Wilson, D., Perry, J., Spitale, J., Brahic, A., Burns, J. A., Del Genio, A. D., Dones, L., Murray, C. D., Squyres, S., (2006). Cassini Observes the Active South Pole of Enceladus, *Science*, 311, 1393-1401.

Raponi, A., Ciarniello, M., Capaccioni, F., Filacchione, G., Tosi, F., De Sanctis, M. C., Capria, M. T., Barucci, M. A., Longobardo, A., Palomba, E., Kappel, D., Arnold, G., Mottola, S., Rousseau, B., Quirico, E., Rinaldi, G., Erard, S., Bockelee-Morvan, D., Leyrat, C., (2016). The temporal evolution of exposed water ice-rich areas on the surface of 67P/Churyumov-Gerasimenko: spectral analysis, *MNRAS*, 462, S476-S490.

Reuter, D. C., Stern, S. A., Scherrer, J., Jennings, D. E., Baer, J. W., Hanley, J., Hardaway, L., Lunsford, A., McMuldroch, S., Moore, J., Olkin, C., Parizek, R., Reitsma, H., Sabatke,

779 D., Spencer, J., Stone, J., Throop, H., van Cleve, J., Weigle, G. E., Young, L. A. (2008).
780 Ralph: A Visible/Infrared Imager for the New Horizons Pluto/Kuiper Belt Mission, *Space*
781 *Science Reviews*, 140, 129-154.

782 Scipioni, F., Schenk, P., Tosi, F., D'Aversa, E., Clark, R., Combe, J.-P., Ore, C. M. D., (2017).
783 Deciphering sub-micron ice particles on Enceladus surface, *Icarus*, 290, 183-200.

784 Shirley, J. H., Dalton, J. B., Prockter, L. M., Kamp, L. W., (2010). Europa's ridged plains
785 and smooth low albedo plains: Distinctive compositions and compositional gradients at the
786 leading side-trailing side boundary, *Icarus*, 210, 358-384.

787 Shkuratov, Y., Kaydash, V., Korokhin, V., Velikodsky, Y., Petrov, D., Zubko, E., Stankevich,
788 D., Videen, G., (2012). A critical assessment of the Hapke photometric model, *Journal of*
789 *Quantitative Spectroscopy and Radiative Transfer*, 113, 2431-2456.

790 Spencer, J. R., Tamppari, L. K., Martin, T. Z., Travis, L. D., (1999). Temperatures on Europa
791 from Galileo Photopolarimeter-Radiometer: Nighttime Thermal Anomalies, *Science*, 284,
792 1514.

793 Stephan, K., Jaumann, R., Wagner, R., Clark, R. N., Cruikshank, D. P., Hibbitts, C. A.,
794 Roatsch, T., Hoffmann, H., Brown, R. H., Filacchione, G., Buratti, B. J., Hansen, G. B.,
795 McCord, T. B., Nicholson, P. D., Baines, K. H., (2010). Dione's spectral and geological
796 properties, *Icarus*, 206, 631-652.

797 Stephan, K., Jaumann, R., Wagner, R., Clark, R. N., Cruikshank, D. P., Giese, B., Hibbitts,
798 C. A., Roatsch, T., Matz, K.-D., Brown, R. H., Filacchione, G., Cappacioni, F., Scholten, F.,
799 Buratti, B. J., Hansen, G. B., Nicholson, P. D., Baines, K. H., Nelson, R. M., Matson, D. L.,
800 (2012). The Saturnian satellite Rhea as seen by Cassini VIMS, *Planetary Space Science*, 61,
801 142-160.

802 Stephan, K., Wagner, R., Jaumann, R., Clark, R. N., Cruikshank, D. P., Brown, R. H., Giese,
803 B., Roatsch, T., Filacchione, G., Matson, D., Ore, C. D., Capaccioni, F., Baines, K. H.,
804 Rodriguez, S., Krupp, N., Buratti, B. J., Nicholson, P. D., (2016). Cassini's geological and
805 compositional view of Tethys, *Icarus*, 274, 1-22.

806 Tosi, F., Mura, A., Filacchione, G., etal. (2018). The Galilean satellites as seen by Juno/JIRAM,
807 *AOGS, 15th Annual Meeting, 03-08 June 2018, Honolulu, USA*, abstract PS07-A025.

808 Trumbo, S. K., Brown, M. E., Fischer, P. D., Hand, K. P. (2017). A New Spectral Feature on
809 the Trailing Hemisphere of Europa at 3.78 $\mu$m, *Astronomical Journal*, 153, 250, 5 pp.

810 Verbiscer, A. J., Peterson, D. E., Skrutskie, M. F., Cushing, M., Helfenstein, P., Nelson, M. J.,
811 Smith, J. D., Wilson, J. C., (2006). Near-infrared spectra of the leading and trailing hemi-
812 spheres of Enceladus, *Icarus*, 182, 211-223.

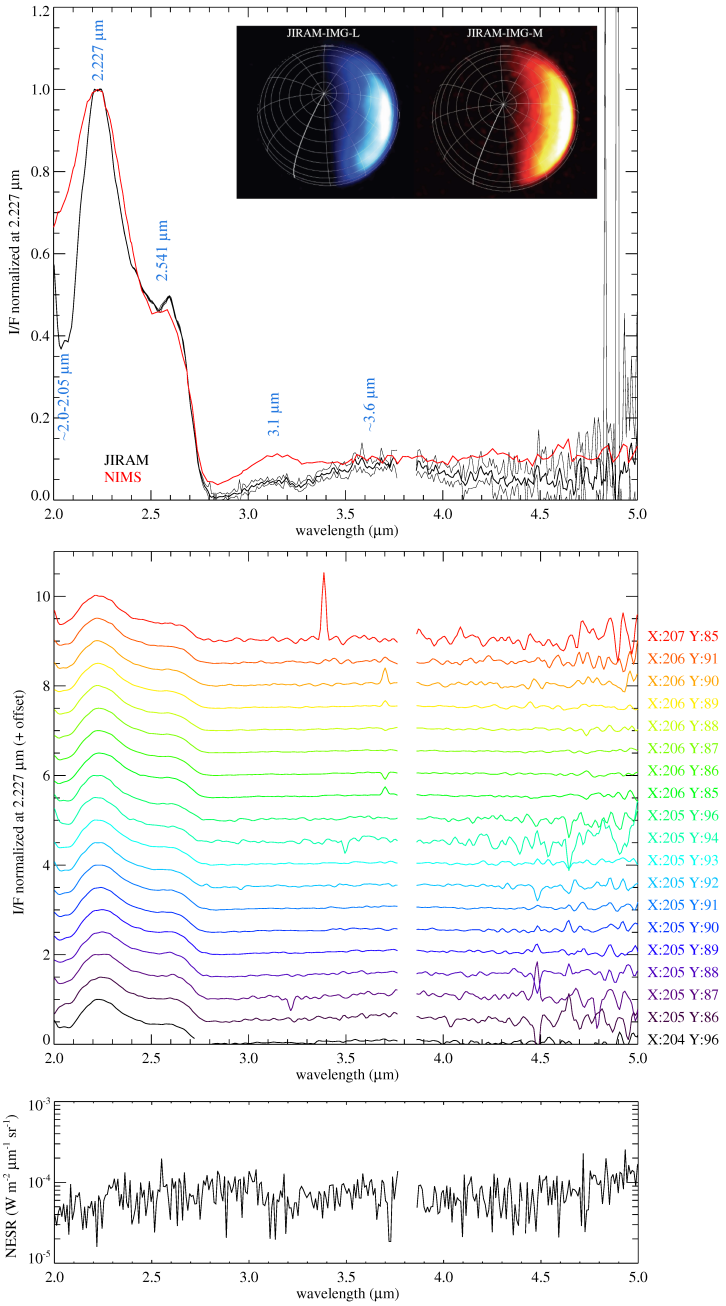


Figure 3: Europa's observation JM0002_160802_213108 on the northern/antijovian hemisphere. Top panel: the plot shows the median I/F spectrum measured by the JIRAM-SPE channel on the dayside fraction of the disk (black curve). The shadowed region shows the instrumental noise. Wavelengths used to derive spectral indicators are labeled and discussed in the text. An observation of Galileo/NIMS acquired on the Europa's north polar region is shown for comparison (red curve). Both JIRAM and NIMS spectra are normalized at 2.227 $\mu$m. The inset panels contain polar projections of concurrent images acquired by the IMG channel in L (3.455 $\mu$m, left panel) and M (4.780 $\mu$m, right panel) bands (*Tosi et al.*, 2018). Centre panel: the 19 individual JIRAM spectra used to compute the average in top panel are compared to NIMS. Bottom panel: JIRAM noise-equivalent spectral radiance (NESR) used to compute the instrumental noise.

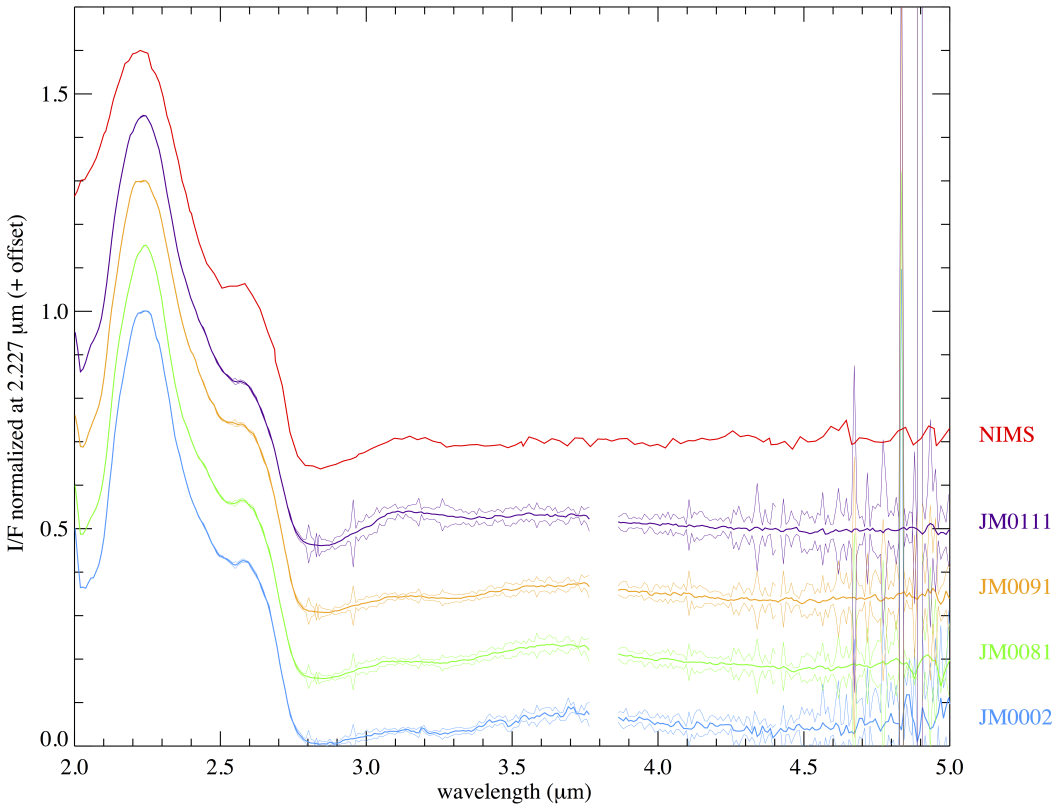


Figure 4: Europa's median I/F spectra collected during orbits JM0002, JM0081, JM0091, JM0111 compared with NIMS.

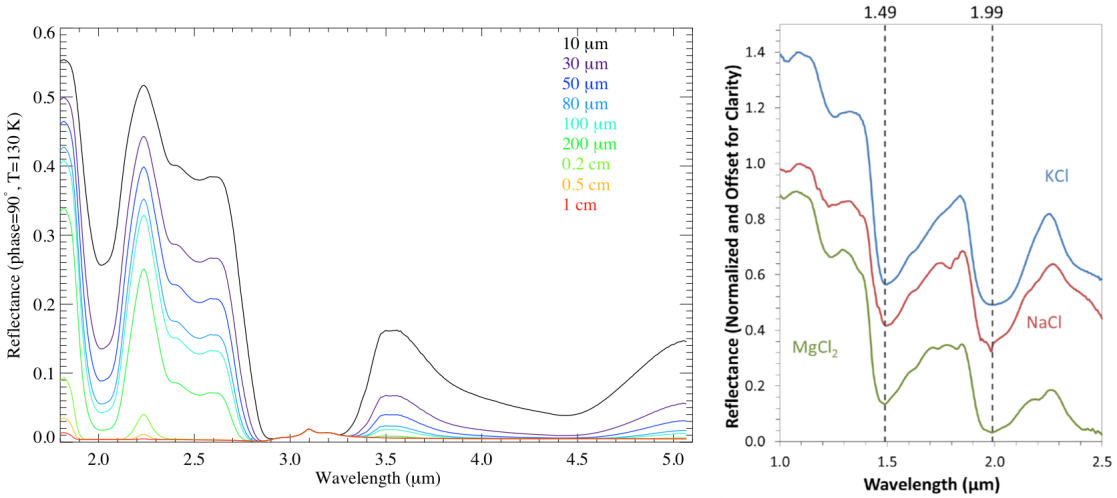


Figure 5: Left: synthetic spectra of water ice grains with sizes between 10 $\mu$m to 1 cm. Right: laboratory reflectance spectra of frozen eutectic chlorine salts $MgCl_2$, NaCl, KCl at T=-30°C (from *Hanley et al.* (2014)).

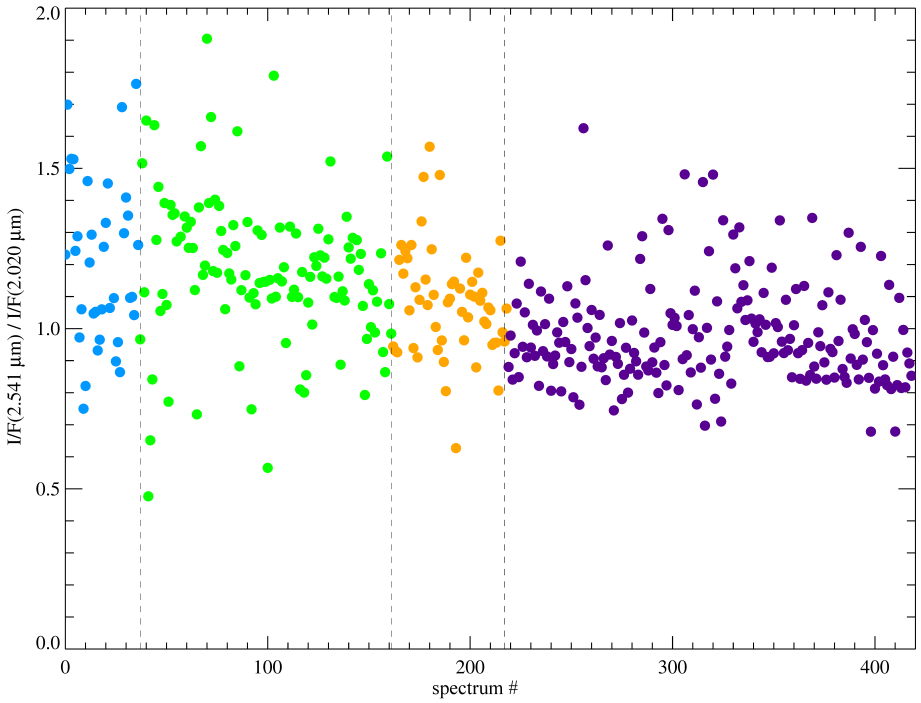


Figure 6: Distribution of the I/F(2.541 $\mu$m) / I/F(2.020 $\mu$m) ratio on the dataset. A ratio similar to 1 is an indicator of the presence of non ice material, like hydrated salts, while larger values correspond to more pure water ice composition. Blue, yellow, green and magenta data points correspond to ratio values measured during orbits JM0002, JM0081, JM0091, JM0111, respectively.

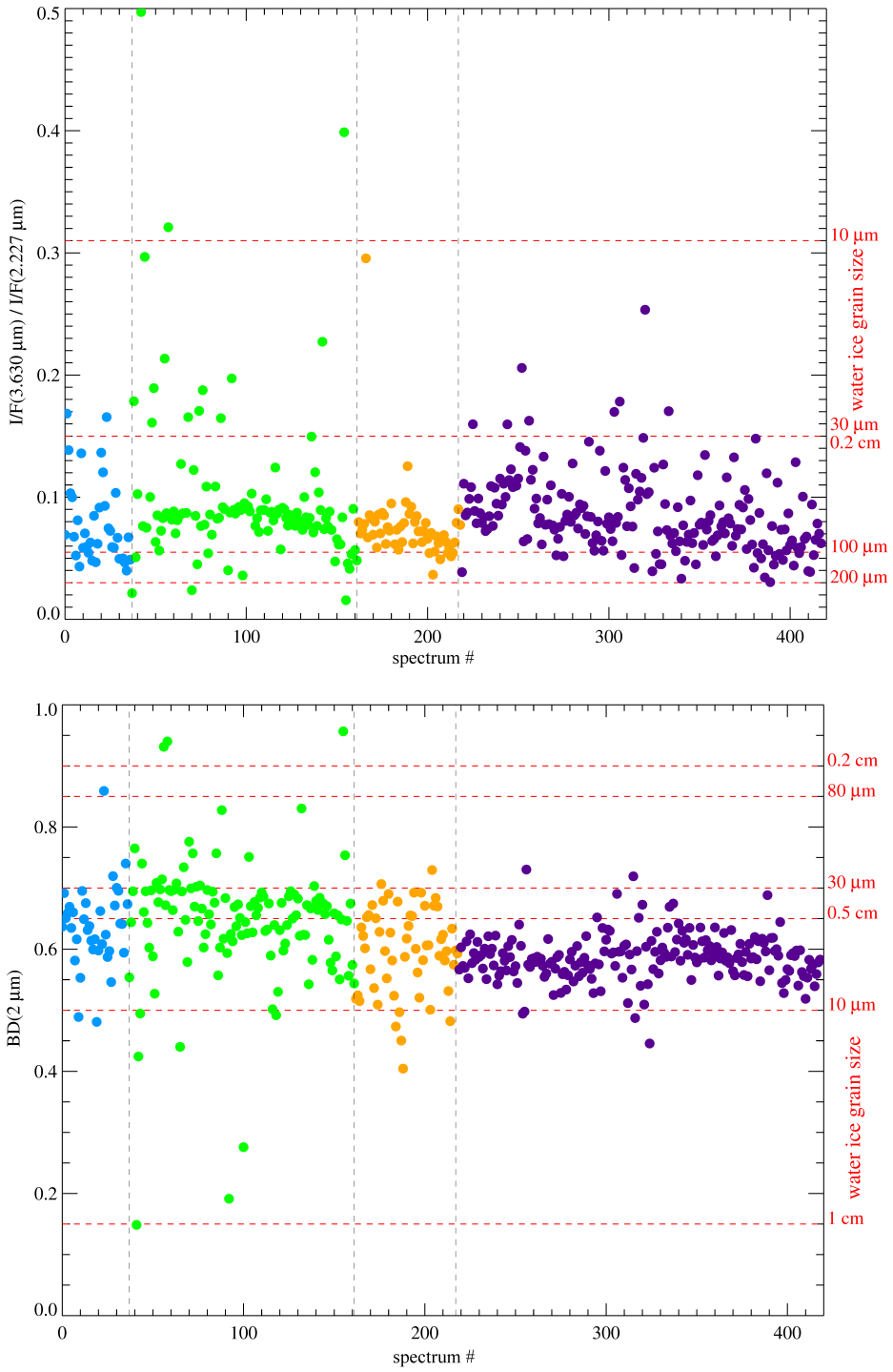


Figure 7: Top panel: distribution of the I/F(3.630 $\mu$m) / I/F(2.227 $\mu$m) ratio in the dataset. Bottom panel: distribution of the BD(2 $\mu$m). Reference grain size values from Table 2 are shown. Blue, yellow, green and magenta data points correspond to ratio values taken during orbits JM0002, JM0081, JM0091, JM0111, respectively.

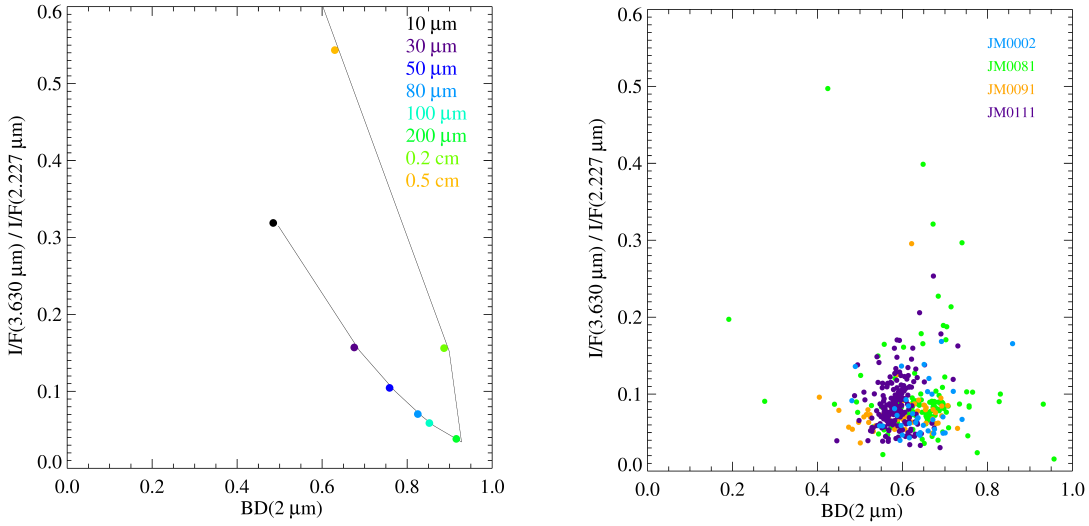


Figure 8: Left panel: trend of the BD(2 $\mu$m) and I/F(3.630 $\mu$m) / I/F(2.227 $\mu$m) as a function of water ice grain size. Right panel: distribution of JIRAM observations.

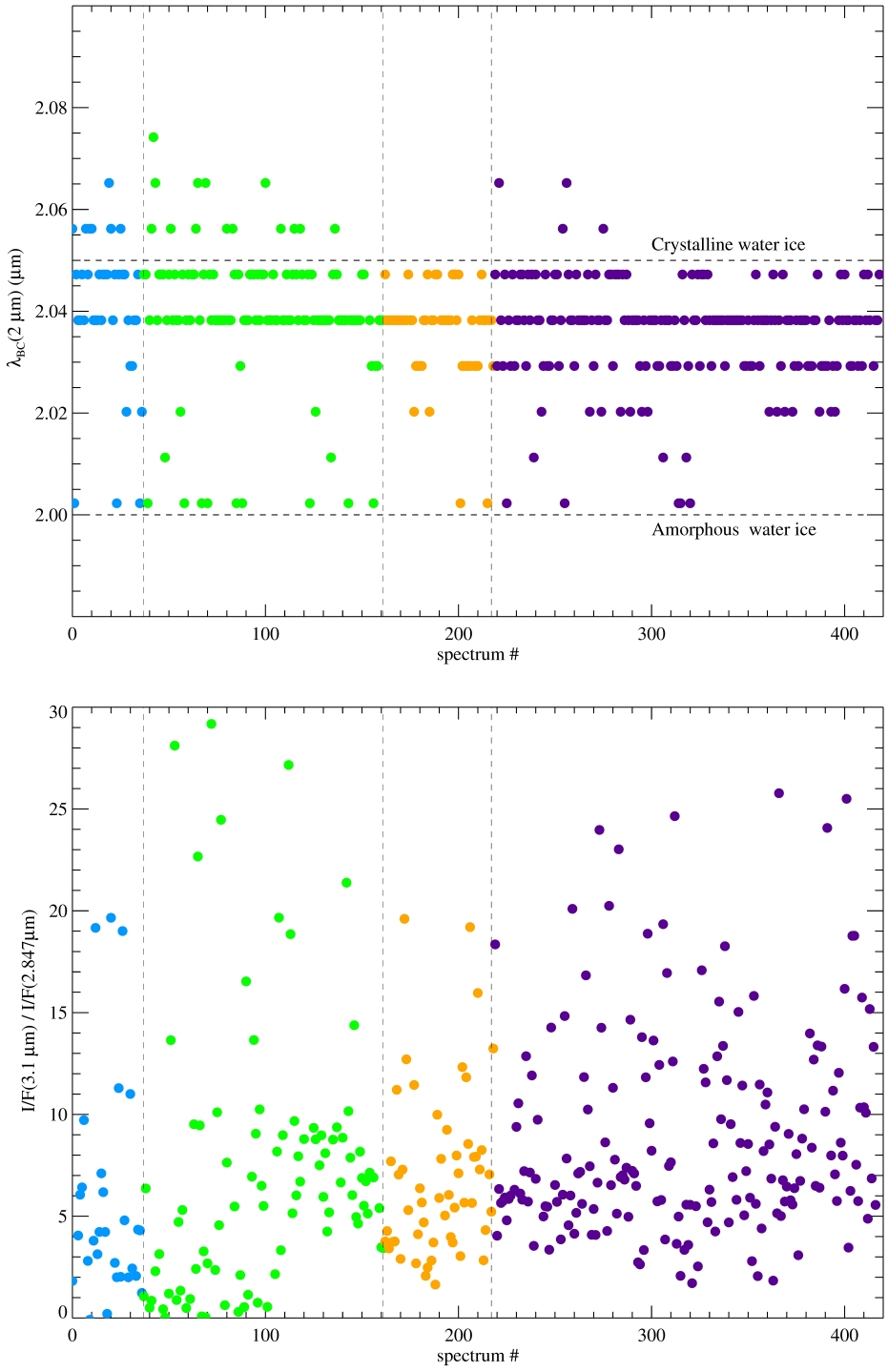


Figure 9: Top panel: distribution of the $\lambda_{BC}(2\ \mu m)$ in the dataset. Reference wavelengths for amorphous and crystalline phases are shown. Bottom panel: distribution of the ratio I/F(3.1 $\mu$m) / I/F(2.847 $\mu$m). High ratio values are indicative of crystalline ice, low ratio values for amorphous ice. Blue, yellow, green and magenta data points correspond to values measured during orbits JM0002, JM0081, JM0091, JM0111, respectively.